http://www.icact.org/journal.asp

ICACT-TACT JOURNAL

Transactions on Advanced Communications Technology

Volume 3 Issue 6, Nov. 2014, ISSN: 2288-0003

Editor-in-Chief
Prof. Thomas Byeongnam YOON, PhD.

GIRI Global IT Research Institute

Volume. 3 Issue. 6

Frequency Offset Estimation for Satellite Communications with Adaptive Frame Averaging

Julian Webber, Masanori Yofune, Kazuto Yano, Naoya Kukutsu, Kiyoshi Kobayashi and Tomoaki Kumagai
Advanced Telecommunications Research International, 2-2-2, Hikaridai, Seika-cho, Kyoto, 619-0288, Japan
{**jwebber, yofune_masanori, kzyano, kukutsu, kumagai**}**@atr.jp**

***Abstract*—The modified Luise and Reggiannini (L&R) algorithm is one of the frequency offset estimation algorithms suitable for use with the Digital Video Broadcasting - Satellite (DVB-S2) standard. Recently we demonstrated an enhanced poly-polarization multiplexing (EPPM) system incorporating L&R frequency recovery as a hardware prototype in order to evaluate its high spectral-efficiency in a real satellite channel. In order to provide sufficient performance at low SNR, it is recommended to average the correlation estimates over 2048 frames. In high SNR regions however, such a large averaging size is unnecessary. In this paper, two techniques are proposed in order to reduce the averaging size. The first technique measures the average noise power and selects an efficient frame averaging length using a noise look-up-table (LUT). The second technique uses a cyclic redundancy check (CRC) to determine if sufficient performance is achievable with the averaging size. Performance results show that the size of the averaging window can be reduced whilst maintaining a target BER. The noise LUT adaptive scheme has been implemented in hardware and we describe the real-time behavior.**

***Keywords*—**satellite communications, polarization multiplexing, frequency offset estimation, latency reduction, performance investigation, hardware implementation.

I. Introduction

High spectral efficiency is especially important in satellite communications due to the constraints of limited transmit power and fixed-bandwidth whilst facing ever-increasing demands on data throughput. The recent DVB-S2X standards extension [1] has brought a number of new design features that increase the spectral efficiency. Increasing the modulation order on each polarization is a common technique to increase the throughput. Although multiple-input multiple-output (MIMO) techniques have revolutionized the mobile communications space, it is less straight-forward to apply them to satellite systems due to the very strong line-of-site channel. In this work, the base-system uses a concept of multiple polarizations, and we focus on the system frequency recovery.

Most modern transponders operate a scheme called orthogonal polarization multiplexing (OPM) in which they simultaneously transmit on vertical (V) and horizontal (H), or lefthand and righthand circular, polarizations and achieve sufficient isolation. Multiplexing more than two signals onto the V and H channels creates interference that cannot be removed by a linear spatial filter as the number of independent paths is limited to two. However, by appropriately selecting the signal constellations at the transmitter and applying powerful digital signal processing techniques at the receiver, it is possible to recover the signals and achieve significant efficiency gains compared to the conventional OPM system.

In general, stricter requirements are made on the phase and frequency recovery algorithms as the modulation order increases. Improved frequency and phase accuracy are therefore becoming important issues with extensions to 256-APSK modulation listed in DVB-S2X and also in our multi-polarization system. Estimation performance can be improved by increasing the UW length and increasing the frame averaging size used in the phase estimation. Here we investigate an adaptive architecture that reduces the frame averaging size while aiming to maintain error performances.

There have been a number of research proposals relating to the optimization of correlation based frequency recovery algorithms. A technique to optimize the correlation length depending on the frequency offset was proposed for the L&R in [2]. In this paper we aim to optimize the frame averaging size, L. We first proposed the adaptive-L by noise estimation (herein termed ALNE) architecture in [3] and we extend that work to describe the hardware performance. In addition, we propose an alternative technique called adaptive-L by CRC (ALC).

This paper is organized as follows. The EPPM technique is briefly introduced in Section II. The frequency estimation and correction method is described in Section III. The ALNE and ALC architectures are detailed in Section IV and V respectively. A software performance investigation is presented

Manuscript received Oct 31, 2014. This work is supported by Japan Ministry of Internal Affairs and Communications with the fund of "Research and Development of Capacity Enhancing Technology for Satellite Communications by Employing Dynamic Polarization and Frequency Control.

J. Webber is with the Wave Engineering Laboratory, Advanced Telecommunications Research Institute International (ATR), Kyoto, 619-0288, Japan. (Tel: +81-774951313; email: jwebber@atr.jp).

M. Yofune is with the Wave Engineering Laboratory, Advanced Telecommunications Research Institute International (ATR), Kyoto, 619-0288, Japan. (email: yofune_masanori@atr.jp).

K. Yano is with the Wave Engineering Laboratory, Advanced Telecommunications Research Institute International (ATR), Kyoto, 619-0288, Japan. (email: kzyano@atr.jp).

N. Kukutsu is with the Wave Engineering Laboratory, Advanced Telecommunications Research Institute International (ATR), Kyoto, 619-0288, Japan. (email: kukutsu@atr.jp).

K. Kobayashi was with the Wave Engineering Laboratory, Advanced Telecommunications Research Institute International (ATR), Kyoto, 619-0288, Japan. He is now with NTT Access Network Service Systems Laboratories, 1-1, Hikarinooka, Yokosuka, Japan. (email: kobayashi.kiyoshi@lab.ntt.co.jp).

T. Kumagai is with the Wave Engineering Laboratory, Advanced Telecommunications Research Institute International (ATR), Kyoto, 619-0288, Japan. (email: kumagai@atr.jp).

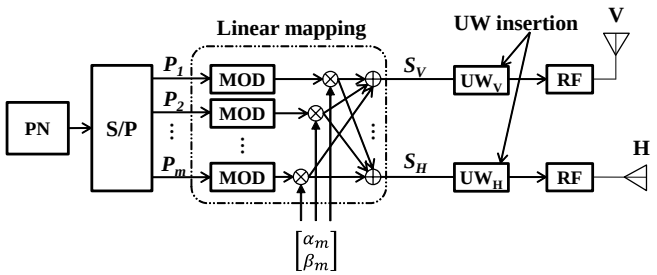

Fig. 1. EPPM transmitter architecture.

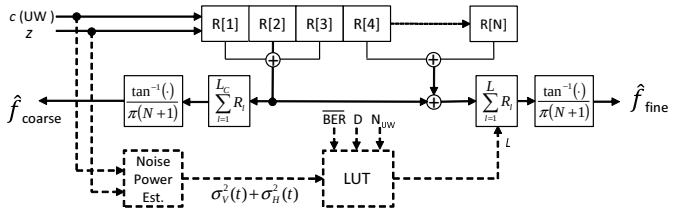

Fig. 2. Block diagram of the frequency recovery showing the additional architecture for noise power estimation with LUT for L.

in Section VI and a discussion of the hardware design in Section VII. Finally a conclusion is drawn in Section VIII.

II. Enhanced Poly-Polarization Multiplexing

The enhanced poly-polarization multiplexing (EPPM) system transmitter architecture is shown in Fig. 1. In the EPPM system, the H and V components of the n-th transmitted symbol, $T_H(n)$, $T_V(n)$ are expressed as

$$\begin{bmatrix} T_H(n) \\ T_V(n) \end{bmatrix} = \sum_{m=1}^{M} \left(\begin{bmatrix} \alpha_m \\ \beta_m \end{bmatrix} X_m(n) \right) \quad (1)$$

where $X_m(n)$ is the m-th stream transmit data symbol to be modulated, α_m, β_m are generalized complex mapping coefficients. An optimized set of mapping coefficients are computed offline by searching for a constellation set that has the maximum minimum-Euclidean distance. The enhanced PPM scheme is a superset that includes the basic PPM scheme. In PPM, a polarization angle between the V and H planes determines the I-Q constellation points on the additional polarization planes. In the simulations in this paper, we transmit on 3 data streams, corresponding to a polarization angle of 45 degrees, with QPSK modulation on each stream. Further details of the technique are described in [4].

III. Frequency offset estimation

In order to estimate the frequency offset and channel state information (CSI), an orthogonal Gold code unique word (UW) is inserted at the start of each frame on V and H polarizations. The UW length is between 64 and 256 symbols is inserted and should be minimized in order to maximize the effective bandwidth efficiency. The target in this paper is to reduce the length from N_{UW}=256 to 64 symbols while maintaining the performance.

The L&R frequency offset [5], $\hat{f}_{LR}$ is estimated from the argument of the sum of correlations, R. The so-called 'modified L&R' computes an average correlation over L preceding frames prior to calculating the argument and improves the performance in noise [6].

$$\hat{f}_{LR} = \frac{1}{\pi T_s (N+1)} \arg \sum_{l=B-L+1}^{B} \sum_{k=1}^{N/2} \frac{1}{N-k} R(k,l) \quad (2)$$

$$R(k,l) = \sum_{i=k+1}^{N} x(i,l) x^*(i-k,l) \quad (3)$$

where T_s is the symbol period, B is the current frame number, $x(i,l)$ is the UW pilot at position i of frame l, and N is the correlation length, N_{UW}/2 in this paper.

The frequency recovery consists of four estimators: a coarse feedback loop and fine feed-forward loop on each of the V and H channels. The architecture of a single-branch is shown by the continuous lines in Fig. 2. The optimum performance of the fine recovery loop is achieved by setting the correlation length equal to half the UW size, as it achieves the Cramer-Rao lower-bound on the estimation error [5]. The coarse loop has a reduced length of between 2-6 symbol delays in order to achieve a large frequency pull-in range.

A. Frame Averaging

The potential benefits of frame averaging were investigated by calculating the average residual frequency offset as a function of the correlation length, N and averaging length, L. The performance of a N_{UW}=256 system, at E_b/N_0=14 dB, symbol-rate 1.6 MBaud and assuming a $\pm$ 3.2 kHz frequency offset on V and H is shown in Fig. 3. It can be seen that the absolute residual offset can be substantially reduced by frame averaging. The residual error reduces at about the same rate with L for a given value of N. The graph shows that it is possible to trade-off L and N in order to achieve a required maximum residual offset. In this work however, we restrict the value of N to half the UW length, in order to simplify an adaptive implementation in hardware. Although the cost of programmable logic memory is now relatively low, it is beneficial to limit excessive values of L particularly in conditions where the offset has high temporal variation. This situation can arise when the phase noise is high or there is movement of, or within the vicinity of, the satellite user-station causing Doppler shift. In a practical system, an average tolerable frequency offset is determined based on the particular quality of service (QoS) requirements. In the next section we propose a method to select L adaptively.

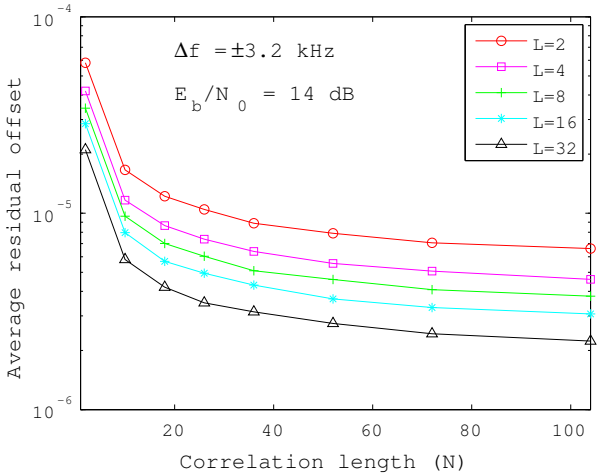

Fig. 3. Average normalized residual frequency offset versus correlation length for different averaging lengths L.

B. Distributed Unique Word structure

In general, frequency estimation performance degrades when shorter UW lengths are used as there are less symbols used and the maximum distance between them is less. We have recently shown that the estimation performance can be improved by increasing the distance between the UW constituent symbols for a given UW length [7]. This technique improves the estimation performance at low values of L and enables the benefits of the adaptive architectures to be further exploited by short UW lengths. The distribution of UW symbols on V-polarization with a constant separation of D=4 are shown in Fig. 4. The data symbols are sandwiched between the UW symbols and the remainder are placed together after the last UW symbol. In the receiver, the distributed UW symbols are repacked into a continuous memory array of length N_{UW}. The frequency estimate is then obtained by dividing the standard L&R estimate with the spacing, D. The variable D is a system-level parameter that needs to be known at both the transmitter and receiver. Therefore it is set at the start-of-packet and remains constant for the entire transmission.

IV. Adaptive-L by Noise Estimation (ALNE)

The frame averaging length is selected based on the average estimated noise power jointly measured on the V and H channels. The basic modified L&R algorithm forms the architecture basis. The additional components comprise a noise estimation process and a look-up table (LUT) containing appropriate averaging lengths. The modifications are indicated by the dashed lines in Fig. 2.

The normalized noise power on each branch, $\sigma^2_{V/H}$ is estimated by subtracting the known transmitted signal component from that of the received signal plus noise. An average value is calculated across N pilots and a sliding-window of W frames

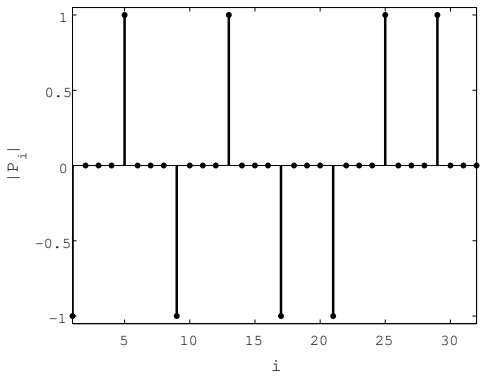

Fig. 4. The first 8 UW symbols with a constant spacing of D=4 separated by data symbols.

TABLE I. ALNE Look-up-table contents.

Index	Lower bound	Upper bound	L
0	0.18	1.00	4096
1	0.12	0.18	1024
2	0.06	0.12	512
3	0.04	0.06	256
4	0.028	0.04	128
5	0.02	0.028	64
6	0.012	0.02	16
7	0.00	0.012	4

as

$$\sigma^2_V(t) = \frac{1}{WN} \sum_{n=t-W}^{t} \sum_{m=1}^{N} |r_V(n,m)|^2 - |r_V(n,m)x^*_V(m)|^2 \tag{4}$$

$$\sigma^2_H(t) = \frac{1}{WN} \sum_{n=t-W}^{t} \sum_{m=1}^{N} |r_H(n,m)|^2 - |r_H(n,m)x^*_H(m)|^2 \tag{5}$$

where, x_V and x_H are the transmitted UW on V and H polarizations, r_V and r_H are the received UW signals on V and H polarizations. An average of the two branches is computed as

$$\sigma^2_{VH}(t) = \frac{1}{2}(\sigma^2_V(t) + \sigma^2_H(t)) \tag{6}$$

The average noise power indexes a LUT containing values of L. The default LUT contains eight entries for the noise boundaries and the associated values for L, as listed in Table I and plotted in Fig. 5. The size of L is a power of two, to make efficient use of reserved memory. Noise boundaries should be pre-computed off-line through a study of BER performance simulations with different L. The LUT can be expanded if more optimal values are determined and can be updated at run-time via a GUI interface.

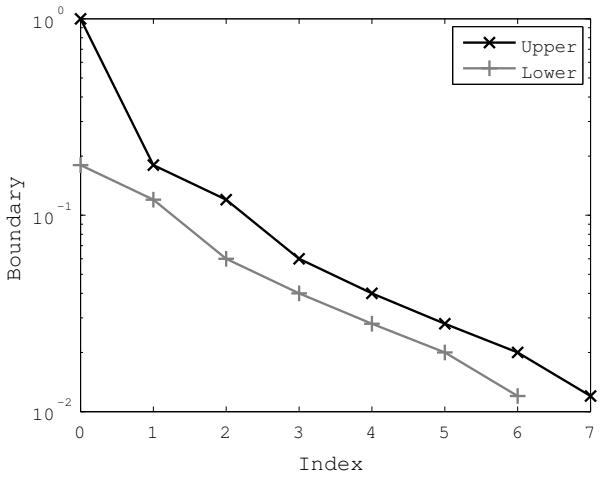

Fig. 5. Plot of the ALNE look-up-table boundaries.

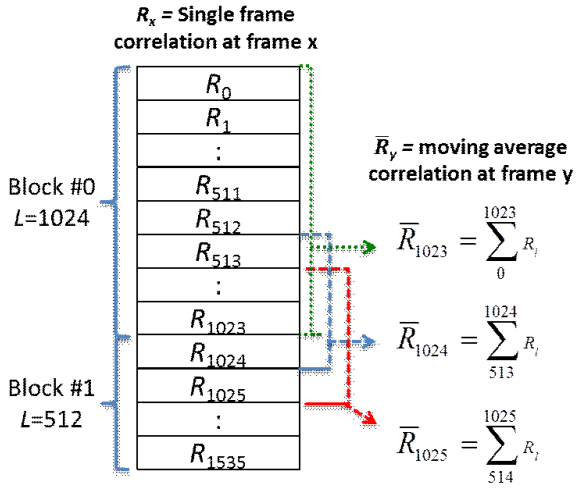

Fig. 6. Calculating the moving average correlation $\bar{R}$ with example of updating the value of L at frame 1024.

At start-up, the memory containing the correlation values is empty and hence the procedure to update L is delayed until the memory buffer is sufficiently full. An example showing the memory structure for the first 1536 frames and associated correlation computations is shown in Fig. 6. The correlation average, $\bar{R}_{1023}$, is computed from frames 0 to 1023 inclusive. After determining the new value of L to be 512, the window is updated to cover frames 513 to 1024. The correlations computed at frames 514 to 1025 are used to calculate the average correlation for frame 1025, and so on.

V. Adaptive-L by CRC (ALC)

In this second architecture, the Tx appends a cyclic redundancy check (CRC) symbol to the end of each frame as shown in Fig. 7. A value of D is set at both the Tx and Rx and is held constant throughout the transmission. At the Rx,

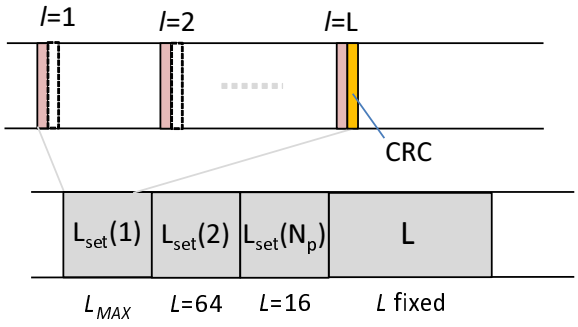

Fig. 7. ALC packet structure showing (top) CRC symbol appended after L frames (bottom) N_L blocks with decreasing value of L followed by transmission with fixed L

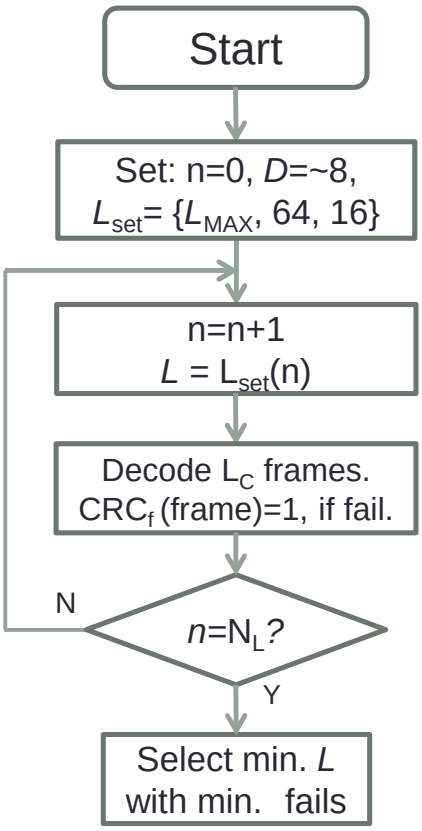

Fig. 8. ALC flowchart for determining the value of L.

a set of L descending values is specified before the start of packet reception, e.g. $L_{set} = \{L_{MAX}, 64, 16\}$, where L_{MAX}, is the maximum value of L to be tested (Fig. 8). It can be set according to the satellite frequency band, D, or MCS. If the channel has a low SNR or a high modulation scheme is used, L_{MAX} is set high e.g. 768. If the channel has high SNR or a high value of D is set, L_{MAX} can be reduced e.g. 128.

After L_{MAX} frames have been received, a frequency estimate is made by averaging the L correlation values.

TABLE II. SIMULATION PROPERTIES.

UW code	Orthogonal Gold
UW length (N_{UW})	64, 256
Data length	2304 symbols / stream
Modulation	3-streams @ QPSK
Freq. offset	±2,4 kHz
Frequency recovery	Modified L&R
Baud rate	1.6M, 3.2M
FEC	None, LDPC (R=5/6)
Channel	AWGN

The l-th frame data is then demodulated and $Rx_{CRC}(l)$ obtained. $Tx_{CRC}(l)$ is then compared with $Rx_{CRC}(l)$. If $Rx_{CRC}(l) \neq Tx_{CRC}(l)$, a CRC fail variable Fail(n) is incremented. Next, $Tx_{CRC}(l{+}1)$ is compared with $Rx_{CRC}(l{+}1)$. Then n is incremented to 1 and the Rx next sets $L{=}L_{set}(1)$. As $L_{set}(1) < L_{set}(0)$ the averaging process, and hence frequency offset estimation, can actually be done using the correlation contents already held in memory and thus without any wasteful retransmissions. The smallest value of L that passes the CRC test is finally selected.

VI. Software Simulation

A performance evaluation was conducted for the EPPM system using the parameters shown in Table II. Random PN data of length 2 bits × 2304 symbols was generated for each of three streams. The stream data was mapped onto the two polarizations using EPPM modulation and a UW preamble inserted of length N_{UW}. The data packet was convolved with a root raised cosine filter having roll-off factor α=0.5. A ± 4 kHz frequency offset was applied to V & H. At the receiver, AWGN is added and the signal matched filtered and down-sampled. The UW sections are extracted and the frequency offsets corrected on both V and H-channels. The noise level is averaged over 32 symbols and indexes the LUT. The data was estimated by MLD processing. The BER measurements started after 2048 frames (i.e. the correlation memory was full for all values of L) and the first value of L had been selected from the LUT.

The BER performance for N_{UW}=64 is plotted in Fig. 9 and shows that when the UW length is short and the UW symbols are adjacent to each other (D=1), the performance is degraded by selecting small values of L. As E_b/N_0 increases however, L can be reduced whilst maintaining a given BER. By increasing the UW symbol spacing to D=8, the performances for low-values of L are substantially improved as shown in Fig. 10. At the BER 1E-4, it can be seen that L can be reduced from 2048 to 128, with a negligeable loss in performance. The BER performance for N_{UW}=256 is plotted in Fig. 11. It can be seen that L can be set to 128 with little performance loss compared to the maximum value.

The required value of E_b/N_0 to achieve an error rate of 1E-4, as L increases for a fixed value of D, is plotted in Fig. 12. A plateau shows the region where there is little additional benefit from increasing the value of L further. It can be seen that

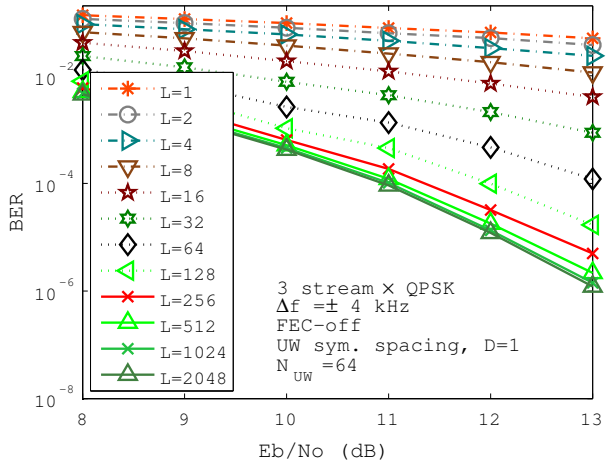

Fig. 9. BER performance of 3 stream × QPSK, N_{UW}=64 with UW symbol spacing D=1.

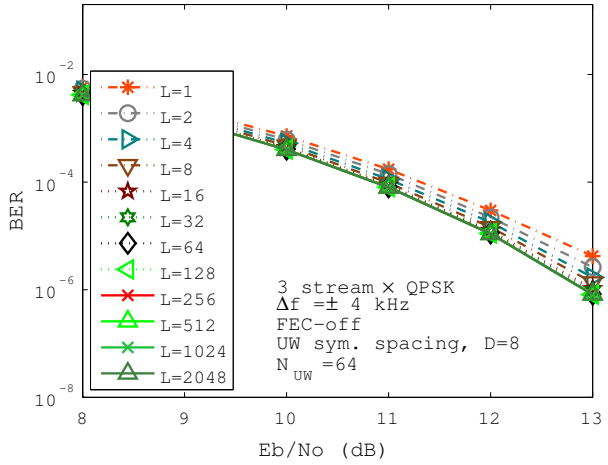

Fig. 10. BER performance of 3 stream × QPSK, N_{UW}=64 with UW symbol spacing D=8.

L=512 is an efficient setting for the case $\{N_{UW}$=64, D=2$\}$. In the case of $\{N_{UW}$=256, D=1$\}$ and $\{N_{UW}$=64, D=4,8$\}$, L can be set to 64 without any observable degradation in performance.

The reduction in the size of L compared to a fixed value of 1024 is shown in Fig. 13 for the case of N_{UW}=64. With symbol spacing D=2, the averaging length can be reduced by about 75% whilst maintaining the target BER at 1E-4. In the case of LDPC with D=4, L can be optimally set to 512 at 4.8 dB and decreased to 32 at 6.0 dB. The optimized settings depend on the particular modulation coding scheme (MCS) and a specific LUT for each MCS should be investigated as part of our future work.

A BER simulation was set-up to investigate the ALC behavior. Three simulations with a different value of D=$\{$8,16,32$\}$ were conducted. At the transmitter, EPPM 6-bit modulation

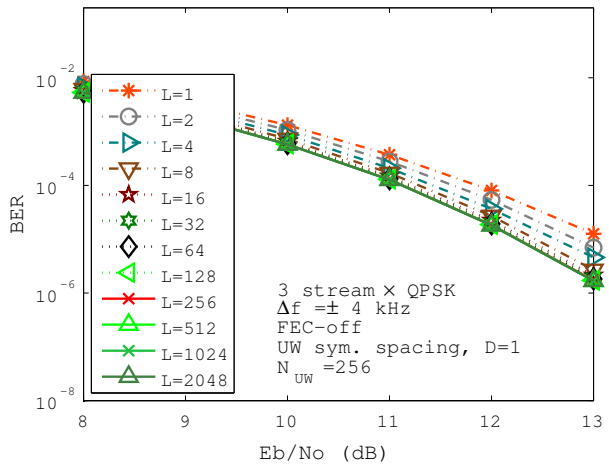

Fig. 11. BER performance of 3 stream × QPSK, N_{UW}=256 with UW symbol spacing D=1.

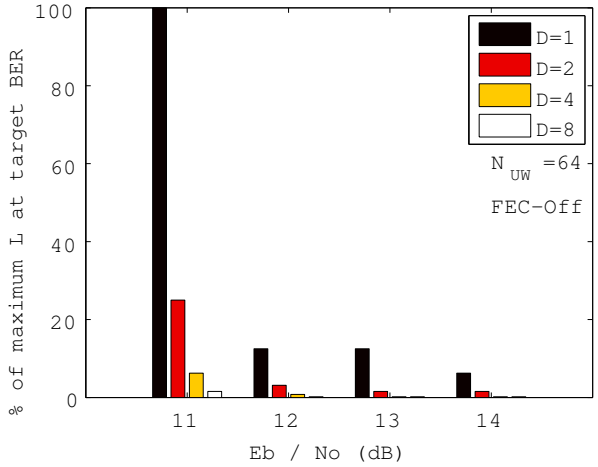

Fig. 13. Percentage in size of L relative to fixing L=1024 whilst maintaining a target BER of 1E-4 for N_{UW}=64 without LDPC.

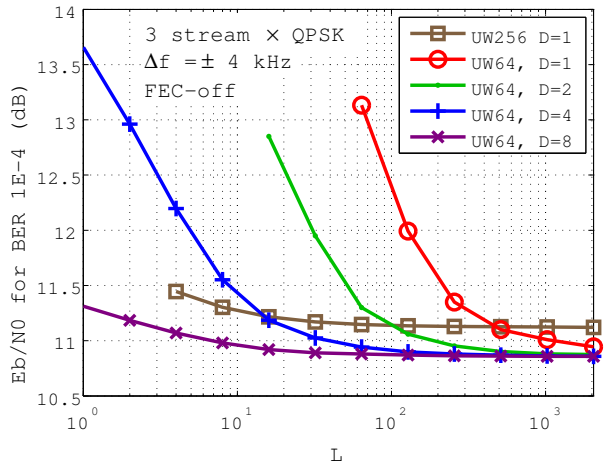

Fig. 12. Required E_b/N_0 to achieve an uncoded BER of 1E-4 as L increases.

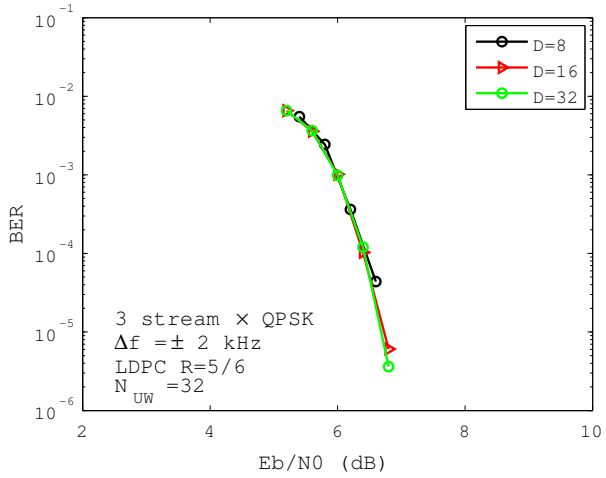

Fig. 14. ALC error performance for D={8,16,32} with ± 2 kHz offset.

with coding rate was R=5/6 was applied. At the receiver, a ± 2 kHz offset was added. The frame averaging size was determined by the adaptive algorithm which selects a value of L that achieves the desired lowest sum of CRC fails. Without, the ALC control, the significantly different D for a fixed value of L would result in different BER. However, the error graph shows that each transmission had almost identical performance (Fig. 14). When a low value of D was used, a larger value of L was selected automatically in compensation.

Both ALC and ALNE use different techniques to achieve the same aim. In terms of complexity, the ALNE is preferred as the noise estimation requires relatively few hardware multiplications and has no CRC overhead. Further, the noise estimation may already be required and computed by the LDPC block. The ALC could however be considered if a CRC module is already part of the system design.

VII. Hardware Implementation

Each transceiver board consists of five Xilinx FPGAs with the frequency recovery and signal processing operations computed on a Virtex XC6SLX100 device. The symbol rate is variable between 0.05-10 MBaud, the input sampling rate is 102.4 MHz. The ADC and DAC precisions were 12-bits and 16-bits respectively. The transmitter and receiver settings are entered via a GUI on the respective Tx and Rx PCs. The required E_b/N_0, frequency and phase offsets were set on a SLE900 satellite channel emulator. The transceiver system is shown in Fig. 15 and further details of the design are in [8]. The BER is computed by comparing the transmitted and received signals using an Anritsu MP8931A BER tester.

The estimated frequency offset on each polarization as measured in hardware is plotted in Fig. 16. The value of D=12 and L was determined by LUT. The estimated offset

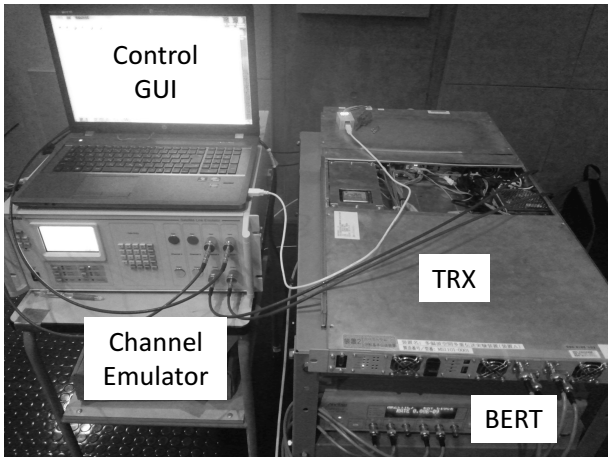

Fig. 15. Satellite testbed system comprising Tx, channel emulator, Rx and BER tester.

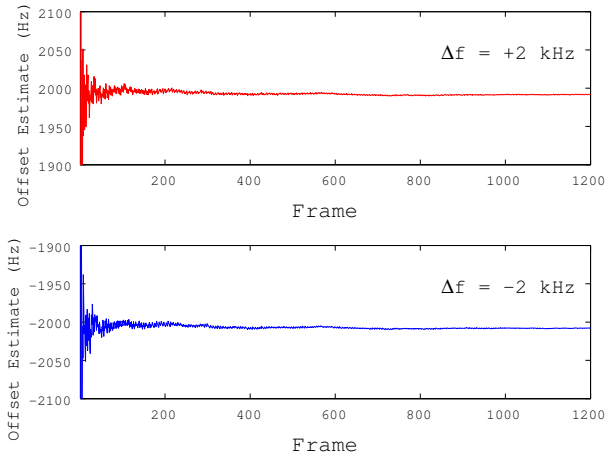

Fig. 16. Frequency offset estimate in hardware in response to a ± 2 kHz offset set by the channel emulator (top) H-polarization, (bottom) V-polarization.

was within ± 8 Hz of the value set in the channel emulator with 10 dB SNR.

A. *Adaptive-L by Noise Estimation*

The LUT in hardware was verified by examining frame versus index results data. The SNR on the SLE channel emulator was varied from 10 dB to 20 dB in steps of 2 dB. The frame number at which the index changed is written to file and from this the variation of L with frame number is plotted in Fig. 17. After switching on the machine, the LUT is filled with correlation data. At position O an SNR of 10 dB is set with the addition switch off in the channel emulator and hence L reverts to the low value of 16. At position A_1, noise addition is switched on and quickly the value of L changes to 1024 at postion A_2. It stays at this position for about 6000 frames. It briefly reduces to 512 but then returns to 1024. At position A_3, the noise is switched off and the value of L rapidly

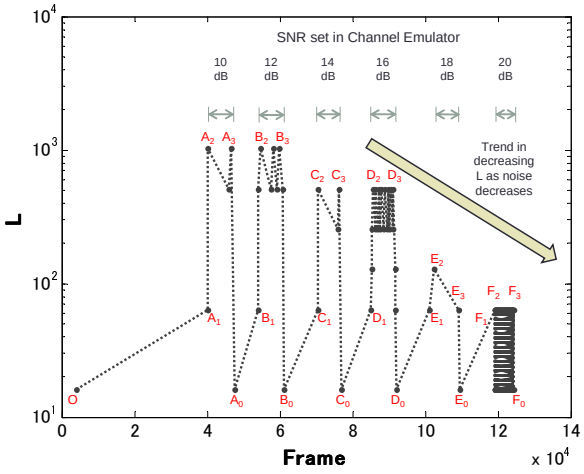

Fig. 17. Variation of L versus frame as SNR increases from ALNE hardware experiment.

reduces to 16. A similar process is repeated for the remaining SNR values. That is, the SNR is set to {12,14,16,18,20} dB at positions $\{B_1,C_1,D_1,E_1,F_1\}$ respectively. The respective noise is added until positions $\{B_3,C_3,D_3,E_3,F_3\}$ respectively.

Two further general observations can be made from this figure. First, there is a downward trend in L observed as the SNR increases and confirms the desired behavior. The exact SNR at which the value of L changes depends on the LUT boundary entries and whose determination is an off-line optimization task to achieve a desired performance. Second, occasionaly (e.g. D_2 to D_3) there are oscillations between two values of L. When L is large, the estimation performance is high and the estimation is very accurate. A lower value of L is subsequently selected by the algorithm. The estimation performance degrades slightly and subsequently a higher value of L is required. To avoid the averaging size being updated too frequently, control circuitry should manage the case when the measured noise power oscillates across a LUT boundary. This situation becomes more important when the LUT is small and thus there are relatively large steps of L.

Various techniques can be applied to control the oscillatory behavior. A hysteresis can be set so that the new setting of L only becomes valid if the boundary is crossed for a sufficient number of frames. Alternatively, the update rate for L can be set to once per a given number of frames. The optimization can also achieved by adjusting the boundary positions or changing the frame averaging LUT entries. This optimization together with the hysteresis should be added as a future upgrade to the firmware. A software simulation with $\{D$=12, L=256$\}$ was compared with hardware results for D=12 with L determined by LUT. There is a close match between the software and hardware performances as shown in Fig. 18. LUT-B achieves slightly better performance than LUT-A due to a larger value of L being used.

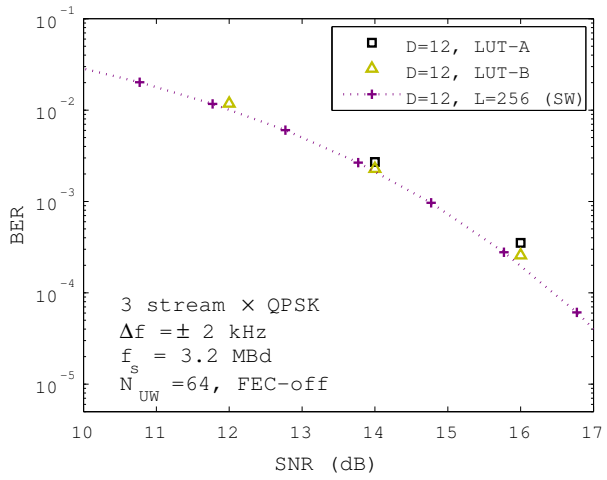

Fig. 18. BER of ALNE in hardware for uncoded 6-bit EPPM with ± 2 kHz offset, 3.2 MBaud, D=12.

VIII. Conclusion

We have proposed two adaptive techniques to reduce the frame averaging required in satellite frequency offset estimation. These techniques are called adaptive-L by noise estimation (ALNE) and adaptive-L by CRC (ALC). In ALNE, the window-size for frame averaging was reduced by selecting it based on the estimated noise power on both V and H branches. A BER of 1E-4 could be maintained with a reduction in L of 75% for D=2 with UW length 64 at 11 dB E_b/N_0. The particular algorithm selection partly depends on implementation complexity and whether CRC and noise estimation modules are already used in other parts of the system. Further work should optimize the performance by adding a hysteresis to avoid excessive switching between boundaries and optimize the averaging sizes for the LUT across a range of MCS and channel conditions.

Acknowledgment

This work is supported by Japan Ministry of Internal Affairs and Communications with the fund of "Research and Development of Capacity Enhancing Technology for Satellite Communications by Employing Dynamic Polarization and Frequency Control."

References

[1] DVB Project Office, "DVB-S2X - S2 extensions: Second generation satellite extensions," *DVB Fact Sheet*, May. 2014.

[2] F. Gong, G. Shang and K. Peng, "Initial estimation based adaptive carrier recovery scheme for DVB-S2 system," *IEEE Transactions on Broadcasting*, Vol. 58, No. 4, Dec. 2012.

[3] J. Webber, M. Yofune, K. Yano, H. Ban, K. Kukutsu and K. Kobayashi, "Adaptive frequency offset estimation for practical satellite communication channels," *IEEE International Conference on Advanced Communications Technology*, Korea, 16-19th Feb. 2014.

[4] M. Yofune, J. Webber, K. Yano, H. Ban, and K. Kobayashi, "Optimization of signal design for poly-polarization multiplexing in satellite communications," *IEEE Commun. Letters*, pp. 2017–2020, vol. 17, no. 11, 2013.

[5] M. Luise and R. Reggiannini, "Carrier frequency recovery in all-digital modems for burst-mode transmissions," *IEEE Trans. Commun.*, vol. 43, no. 2/3/4, pp. 1169–1178, Feb-Apr. 1995.

[6] ETSI "Digital Video Broadcasting (DVB) User guidelines for the second generation system for broadcasting, interactive services, news gathering and other broadband satellite applications (DVB-S2)," *ETSI Technical Document TR 102 376 v1.1.1*, Sophia Antipolis, Feb. 2005.

[7] J. Webber, M. Yofune, K. Yano, H. Ban, and K. Kobayashi, "Performance of frequency recovery algorithms for a poly-polarization multiplexing satellite system," *IEEE Malaysia International Conference on Communications (MICC'13)*, Malaysia, Nov. 2013.

[8] J. Webber, M. Yofune, K. Yano, H. Ban, and K. Kobayashi, "Experimental evaluation of a poly-polarization multiplexing system with timing/frequency recovery for satellite communications," *AIAA International Communications Satellite Systems Conference (ICSSC'13)*, Florence, Italy, Oct. 2013.

Julian WEBBER received the M.Eng. and Ph.D. degrees from the University of Bristol, UK in 1996 and 2004 respectively. From 1996-98, he was with Texas Instruments, Europe engaged on ASIC and DSP systems. From 2001-07 he was employed as a Research Fellow at Bristol University engaged in real-time MIMO-OFDM testbed implementation, and from 2007-12 he was a Research Fellow at Hokkaido University, Sapporo, Japan, working on MIMO signal processing & wireless communications. He is currently a researcher at ATR, Kyoto, Japan principally working on frequency recovery and spectrally efficient modulation techniques for satellite communications. His other current research interests include MIMO, high resolution direction of arrival estimation and M2M. He is a member of the IEEE and IEICE.

Masanori Yofune received the B.E. and M.S. degrees in systems engineering from Hiroshima City University, Hiroshima, Japan, in 2008 and 2010, respectively. In 2010, he joined Mobile Techno Corporation, Kawasaki, Japan, where he has been engaged in research and development on wireless communication systems. In 2012, he was assigned to ATR Wave Engineering Laboratories as a researcher and engaged in research and development on advanced techniques for frequency efficiency in satellite communication systems. His interest areas are wireless communication systems and digital signal processing. He is a regular member of the Institute of Electronics, Information and Communication Engineers (IEICE) of Japan.

Kazuto Yano received a B.E. degree in electrical and electronic engineering, M.S. and Ph.D. degrees in communications and computer engineering from Kyoto University in 2000, 2002, and 2005, respectively. He was a research fellow of the Japan Society for the Promotion Science (JSPS) from 2004 to 2006. In 2006, he joined the Advanced Telecommunications Research Institute International (ATR). Currently, he is a senior research scientist of the Wave Engineering Laboratories, ATR. His research interests include space-time signal processing for interference suppression, MIMO transmission, and PHY/MAC cross-layer design of cognitive radio for ISM bands. He received the IEEE VTS Japan 2001 Researcher's Encouragement Award, the IEICE Young Researcher's Award in 2007, the Ericsson Young Scientist Award 2007 and the IEICE 2007 Active Research Award in Radio Communication Systems. He also received 2010 Young Investigator Award in Software Radio from IEICE Technical Committee on Software Radio. He is a member of IEEE and IEICE.

Naoya Kukutsu received the B.E., M.E., and D.E. degrees in electrical engineering from Hokkaido University, Sapporo, Japan, in 1986, 1988 and 1991, respectively. His D.E. dissertation described research for a time-domain electromagnetic wave numerical analysis method. In 1991, he joined the Nippon Telegraph and Telephone Corporation (NTT), Applied Electronics Laboratories, and was engaged in developing high speed IC packages. From 2008-2013, he was a senior research engineer, supervisor at NTT Microsystem Integration Laboratories, and leader of the group that develops millimeter-wave and terahertz-wave radio transmission, as well as imaging systems. He is currently a senior research engineer at ATR Wave Engineering Laboratories and head of the department of Environment Communications. Dr. Kukutsu is a member of the IEEE MTT and COM Societies and a senior member of the Institute of Electronics, Information and Communication Engineers (IEICE).

Kiyoshi Kobayashi received the B.E., M.E. and Ph.D. degrees from Tokyo University of Science, Japan, in 1987, 1989 and 2004, respectively. He joined NTT Radio Communication Systems Laboratories in 1989. Since then, he has been engaged in the research and development of digital signal processing algorithms and their implementation techniques including modem, synchronization control and diversity for satellite and personal wireless communication systems. From 2011 to 2014, he was the director of ATR Wave Engineering Laboratories at Advanced Telecommunications Research Institute International, where he was engaged in research on advanced technologies for wireless communications. Currently, he is a senior research engineer, supervisor and a group leader of Satellite Communication Group in NTT Access Network Service Systems Laboratories, working on development of satellite communication systems. He is a member of IEEE and IEICE.

Tomoaki Kumagai received the B.E. and M.E. degrees in Electrical and Communication Engineering, and Ph.D. degree in Information Science from Tohoku University, Sendai, Japan, in 1990, 1992 and 2008, respectively. Since joining NTT in 1992, he has been engaged in research and development of personal communication systems and high-speed wireless LAN systems. Since 2014, he is the Director of Wave Engineering Laboratories, Advanced Telecommunications Research Institute International (ATR). He received the Young Engineer Award from the Institute of Electronics, Information and Communication Engineers (IEICE) in 1999. He is a member of the Institute of Electronics, Information and Communication Engineers (IEICE) and IEEE.

Radio Propagation Characteristics in the Large City and LTE protection from STL interference

YoungKeun Yoon, JongHo Kim, MyoungWon Jung, YoungJun Chong

Radio Technology Research Department, ETRI, Republic of Korea

ykyoon@etri.re.kr, jonghkim@etri.re.kr, mwjung@etri.re.kr, yjchong@etri.re.kr

***Abstract*— This paper describes composite propagation effects of both the median pathloss and shadow fading in the large city. In general, the propagation characteristic for the power profile of received signal has the relative power reduction and fluctuation according to distance to the receiver's location far away from the transmitter. The result of these channel propagation losses is due to the reduction of electric field in the air according to the separated distance between a transmitter and receiver, and due to the multipath effect such as the plane reflection and edge diffraction of the propagated radio signals at the plane of buildings and roads or vehicles etc. Propagated multipath radio signals via different paths may be simultaneously received to a target receiver with different field strength and phases. Actually, it is not easy to how to predict the optimum radio propagation characteristics in the large city from a transmitter to target receiver at the specific mobile or fixed communication link, because the outdoor environment have the different height of transceivers and various structure factors such as buildings, roads, and vehicles in the large city including the urban, suburban and rural area. Therefore, the measurement is currently candidate solution for predicting the radio propagation characteristics in the novel environments. In this paper, two different stations between a fixed and mobile station are considered. Measurement results are compared with the general radio propagation model of 3GHz frequency and lower. As another issue, we discuss and propose on the closed form of the interfering received signal strength intensity when two different stations like a fixed system as the repeater and a mobile system as Long Term Evolution coexist in the same area. In the coexisting environment, two different stations overlap the cell coverage and are assigned in the adjacent channel frequency. Therefore, the potential interference may cause to their reception each other. Here, it is important to analyze the interference impact to the victim station as a receiver from the interfering station as a transmitter to get out of the interference. In this paper, it is assumed that an interfering station as a transmitter is fixed repeater and a victim station as a receiver is a mobile Long Term Evolution system. For estimating interfering received signal strength intensity, it is issued to figure out a radio propagation characteristic. However, it is unknown for the available median pathloss model to apply for analyzing the performance of Long Term Evolution system from interfering fixed repeater in the large city with none line of sight in the coexisting environment. Finally, we propose the median pathloss characteristic from measuring the electric field strength of a fixed repeater as an interfering transmitter and calculated interfering received signal strength intensity to a victim station. Using both the measurement and the theoretic calculation results, the separated distance between an interfering transmitter and victim receiver is discussed for the protection of a victim station.**

***Keyword*— interference, wave, pathloss, fading**

I. INTRODUCTION

LONG Term Evolution (LTE) has been developing to transport increasing traffics of mobile communication data [1]. Studio transmitter link (STL) station does transport a radio station's audio data from the broadcast studio to a repeater in another location. The transmitter studio link (TSL) is the return link, which transports telemetry data from remotely located a repeater back to the broadcast studio. STL and TSL station are a kind of the fixed microwave link station. Figure 1 shows the frequency allocation and arrangement between STL and LTE uplink bands. Two stations operate each other in adjacent frequency bands. Let us consider the potential LTE interference impact from STL station's emission at 1.7GHz frequency bands in the coexisting case both LTE base station and STL system in the same service area.

In this situation, the analysis and its results on the potential LTE performance impact due to the interference of STL station in the large city were not known to us, yet. Therefore, we tried to derive a theoretic LTE interference impact from the harmful power of STL station in the adjacent frequency bands.

Fig. 1. Frequency assignment of both STL and LTE uplink.

To calculate interfering STL and desired LTE station's received signal strength intensity to the LTE reception, let us consider theoretic median pathloss and shadowing model, because interfering or wanted transmitter power is reduced by the separated distance between a transmitter and a victim

Manuscript received November 1, 2014. This work was supported by the ICT R&D program of MSIP/KCA. [2013-005-036-001, Wireless Channel and Frequency Characterization based on Field Measurements for Broadband Mobile Hot-Spot Applications]

Y. Yoon is with radio technology research department, Electronics and Telecommunications Research Institute, Daejeon, Republic of Korea (email: ykyoon@etri.re.kr)

J. Kim is with radio technology research department, Electronics and Telecommunications Research Institute, Daejeon, Republic of Korea (email: jonghkim@etri.re.kr)

M. Jung is with radio technology research department, Electronics and Telecommunications Research Institute, Daejeon, Republic of Korea (email: mwjung@etri.re.kr)

Y. Chong is with radio technology research department, Electronics and Telecommunications Research Institute, Daejeon, Republic of Korea (email: yjchong@etri.re.kr)

receiver. In addition, radio propagation characteristic varies to the outdoor environment factors such as building, ground, and etc.

In this paper, general radio propagation models in the various environments like urban, suburban, and open area are considered. Extended Hata model is general and feasible median pathloss model within lower than 3GHz frequency bands in the mobile communication service. Extended Hata model is used to calculate pathloss according to the separated distance in none line of sight (NLOS) as well as line of sight (LOS) environment [2]. In the free space environment case, reference ITU-R P.525 model is available to calculate the median pathloss between a wanted transmitter and desired receiver in open area [2]. In referred [1]-[2], using median pathloss and long term fading characteristics with log-normal distribution, we can calculate available cell area corresponding to the minimum sensitivity level of desired receiver. If referred general model of [1]-[2] are always good in agreement with measurement results, we could use theoretic median pathloss model and shadowing value without waste time for long measurement process and database analysis. However, composite median pathloss and shadowing characteristics according to separated distance in the large city including dense urban and suburban environment was not known to us. Therefore, we measured radio propagation characteristics in the large city and found various median path loss characteristics, when STL station transmits the audio data from the broadcast studio to a repeater in another location. Currently, the median path loss value getting from the referred theoretic model [1]-[2] is not a good match with our measurement results in the specific environment like the large city including the dense urban and suburban, because theoretic median path loss model is very general model in the specific site environment and is not good agreement with all environments. Also, a choice of the median pathloss model for the link budge calculation on the transceiver station is not difficult. For example, mobile operators choose Extended Hata model within lower than 3GHz frequency bands for calculating the site coverage in macro or micro or hotspot environment. In the other hands, TV broadcasters use the reference ITU-R P. 1546 model in the point to multi point environment with time varying and spatial rates of the radio signal profile [3]. However, this simple choice may happen a large error in the specific environment like the large city including the dense urban and suburban. This error may happen to inaccurate the median pathloss calculation and we could have faults calculating an interference impact to the LTE reception in the adjacent frequency bands from an interfering STL signal power.

Actually, for the link budge calculation, the mobile LTE operators use Extended Hata model in the LOS and NLOS environment in the urban or suburban. The other fixed STL microwave broadcasters use the free space loss model in the open area and the reference ITU-R P. 1546 model in the LOS and NLOS environment over the coverage of 1km and higher. This is the reason that each mobile or fixed station's environment has different conditions, which they include the transmitter antenna height, the receiver antenna height, the transmission distance, and the receiver sensitivity, etc.

In this paper, we talks to derive the composite median path loss and shadowing value for the LTE protection from the interference impact of interfering STL transmitter. As an approach, we measured the transmission power of STL station during moving with a vehicular from the STL broadcast studio to a repeater in another location. The measurement frequency is at 1.7GHz bands and it is within in-bands of LTE bands at the adjacent STL frequency bands. As the fixed STL microwave broadcasters, we considered two stations with different link paths in the large city. One STL station is Far East Broadcasting Company (FEBC) and, while the other is Seoul Broadcasting Station (SBS).

Finally, we found to shall be used composite median pathloss with shadow fading to correspond to various urban, suburban, and rural environments in the large area. Measurement results are in good match with the results of composite different median pathloss models of various urban and suburban.

II. STATION PARAMETERS

To calculate interfering transmitter and desired LTE received signal strength intensity to a LTE reception, let us consider fixed STL with wireless services as interfering transmitter.

Fixed wireless service utilizes a transmission tower similar with a cell phone tower on the top of the building. The equipment installed upon transmission tower communicates with one of a repeater for the wireless transmission of the information data. STL station as a transmitter station means a kind of the transmission tower providing the fixed service and does transport a radio station's audio and video data from the broadcast studio to a repeater in another location. A repeater as a receiver installs the transceiver equipment on the top of mountain to communicate with a fixed wireless broadcast studio on the top of buildings in the city. A repeater and the broadcast studio include a grid meshed or dish shaped antenna connected to the radio transceiver. The antenna beam of the broadcast studio should be faced to the pointing direction of a repeater for LOS access to reduce pathloss between a transmitter and receiver. This is the reason that the obstructions of a hill and several high buildings can adversely affect to the performance impact of the quality of service (QoS). As the fixed STL microwave broadcasters operating at 1.7GHz frequency bands [4]-[7], we considered two stations with different link paths in the large city. One STL station is FEBC and, while the other is SBS. The STL transmitter sends the radio station's audio analogue or digital data from the broadcast studio transmitter to the radio transmitter operating as a receiver in another location. STL radio links can be analogue or digital type and considered broadcast auxiliary services (BAS). Table 1 shows system parameters of STL stations and these values are assumed.

SBS is digital type and FEBC's station is the older analogue system. Two STL stations operate in the frequency of 1.7GHz bands with the channel bandwidth of 230 kHz. Antenna type is the same grid parabola with 26dBi including the feeder loss of 2dB. The antenna height (sea level) of the FEBC and SBS transmit station is 35m or 70m, relatively. The antenna height (sea level) of receiving station is the same height of 625m. Receiver is located in the tower of on the top

of Mt. Gwanaksan. The antenna 3dB beamwidth of STL stations is 6.5degree in the elevation axis as shown in Figure 2.

Table 2 shows system parameters of LTE station and these

TABLE I
STL STATION PARAMETERS [4] –[7]

Parameters	FEBC (TFT8300)	SBS (SL9003)
Analogue/Digital	Analogue	Digital
Channel bandwidth (㎑)	230	230
Transmit power (W)	5.0	1.0
Operating frequency (㎓)	1.7GHz bands	1.7GHz bands
Antenna gain (dBi)	26 (grid parabola)	26 (grid parabola)
Antenna HPBW (degree)	6.5 (elevation)	6.5 (elevation)
Antenna height (m)	Transmitter 35 Receiver 625	Transmitter 70 Receiver 625

TABLE II
LTE STATION PARAMETERS [8]

Parameters	Values	Units
Downlink peak rates	100	Mbps
Uplink peak rates	50	Mbps
Transfer latency	< 5	msec
Scalable carrier channel bandwidth	1.4~20	㎒
Duplexing	FDD	
Antenna gain	15	dBi
Antenna HPBW	7.0 (elevation)	degree
Antenna downtilt	-3	degree

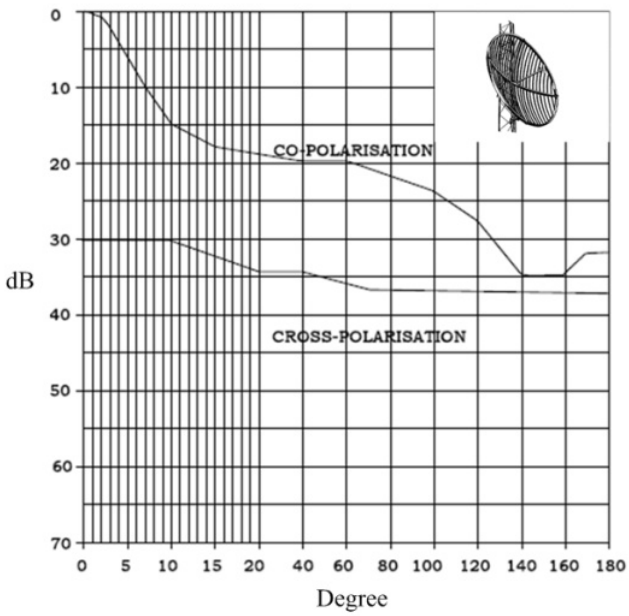

Fig. 2. STL station's antenna elevation pattern (e.g. grid parabola) [4].

values are assumed.

LTE base station supports moving mobiles, and multi-cast as well as broadcasting data. We assumed the channel bandwidth of 5MHz x 2 supporting the frequency division multiplexing (FDD). LTE stations operate in the frequency of 1.7GHz bands. Antenna type is the linear antenna with x-polarization and with 15dBi gain including the feeder loss of 3dB. Antenna height (sea level) of LTE base station is 15m. LTE base station is a receiver in the uplink. The antenna 3dB beam-width of LTE station is 7.0degree in the elevation axis as shown in Figure 3.

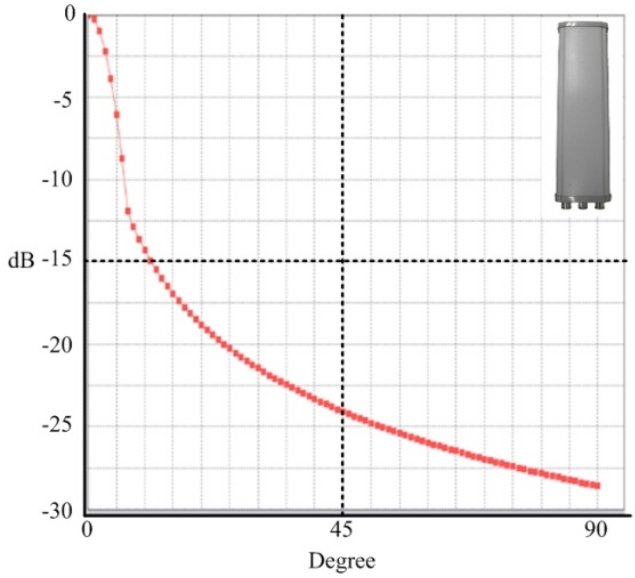

Fig. 3. LTE base station's antenna elevation pattern (e.g. Linear) [4].

III. MEASUREMENTS

A. Measurement Path

We assumed coexisting scenarios between STL and LTE station in the large city. The antenna height (sea level) of FEBC and SBS transmit station is 35m or 70m as shown in the Table 1, relatively. The antenna height (sea level) of LTE base station is 15m in the Table 2. STL transmit stations are assumed as the interfering transmitters and LTE base station is assumed as a victim receiver to protect from the interfering STL transmit stations. To derive the interfering received signal strength intensity to LTE base station receiver, we tried to find the available median pathloss model in the case of both the transmitter antenna height of 35m and higher, and the receiver antenna height of 15m and higher. However, we didn't look for the available radio propagation characteristics. Finally, we measured the median pathloss characteristics and calculated interfering received signal strength intensity to a victim LTE base station. Using both measured and theoretic calculation results, the separated distance between the victim station and interfering station is discussed for the protection of a victim station. Figure 4 shows the STL link (Link 1) of FEBC transceiver between the broadcasting transmit station on ground and receiving station on the top of Mt. Gwanaksan. The measurement of FEBC transmit power was performed within the measurement region 1 during moving the car in the large city. Figure 5 shows the STL link (Link 2) of SBS transceiver between the broadcasting transmit station on ground and receiving station on the top of Mt. Gwanaksan. The measurement of the transmit power of SBS was performed within the measurement region 2 during moving the car in the large city. The distance of Link 1 and Link 2 in a straight line between the transmit antenna pointing of the broadcasting transmit station and receiver antenna pointing of the receiver is about 10km and 12.4km, respectively.

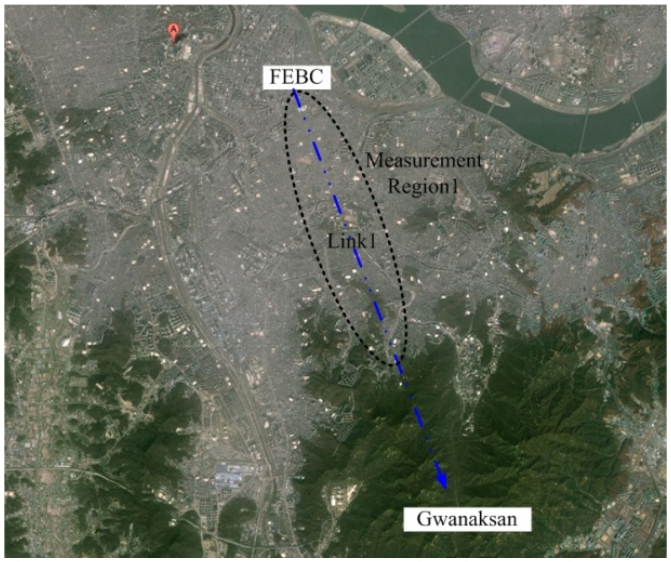

Fig. 4. Measurement route I (e.g. FEBC tansmit station to a receiver on Mt. Gwanaksan) [4].

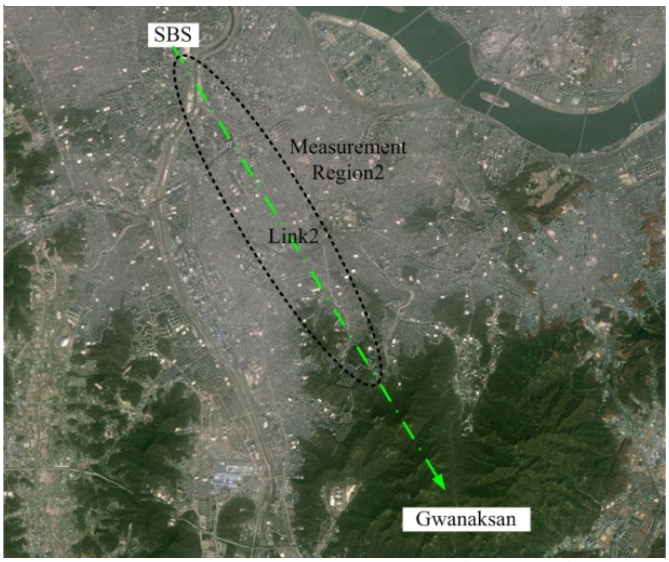

Fig. 5. Measurement route II (e.g. SBS transmit station to a receiver on Mt. Gwanaksan) [4].

B. Measurement Environment

Figure 6 shows the measurement scenario using a vehicular in order to measure the median pathloss and long term fading characteristics at 1.7GHz bands in the large city.

Measurement was performed on road in the large city including huge or small buildings and hills with moving car from the STL transmit station. A car with the measurement system has been moved from the STL transmit station (Transmitter) to near by the front of the STL receiving station (Receiver) on the top of Mt. Gwanaksan. The measurement system includes the vector network analyzer, the low noise amplifier, the band-pass filter, and the omni antenna. The antenna height (h_v) on the top of a car is 2.5m. We defined the antenna height of STL station as follows; STL transmit antenna height is H_1 and STL receiving antenna height on the top of Mt. Gwanaksan is H_2.

IV. Results & Analysis

A. General Median Path loss Models

For comparing measurement with theoretic analysis results, we looked for the general candidate median pathloss model. [2], [4]

In this model, for line of sight in the open area, the free space model is used.

$$PL_{FSL}(dB) = 10\log\left\{\left(\frac{4\pi}{c} d_1 f\right)^2\right\} = 32.44 + 10\log\left\{\left(\frac{H_1 - h_v}{1000}\right)^2 + d^2\right\} + 20\log(f) \quad (1)$$

The free space pathloss is proportional to the square of the separated distance in km between the radio transmitter and radio receiver. In addition, it is proportional to the square of the operating frequency in the unit of MHz of receiver in (1). Free space pathloss is the minimum radio propagation loss in the signal strength of electromagnetic wave that would result from the unobstructed direct line of sight path through the air in the open area. Free space pathloss is examples applied to the fixed microwave link or broadcasting link or telecommunication link over the short distance in the open area, etc.

For the telecommunication link operating at 3GHz and lower bands, Extended Hata model is typically used. Extend Hata pathloss is the radio propagation loss in the signal strength of electromagnetic wave that would result from the obstructed none line of sight as well as the unobstructed line of sight path through the air in the urban, suburban, and rural area. Extended Hata model was developed by European study committee (COST 231). This model is an extension of Okumura-Hata model, being applicable for the frequency to 3GHz and lower bands, with receiving antenna heights from 1m to 10m and the transmitting antenna heights of 30~200m. It is used for the prediction of pathloss for mobile wireless system in urban, suburban, and rural environments.

In case of urban environment,

$$PL_{Urban}(dB) = 46.3 + 33.9\log(f) - 13.82\log(\max\{30, H_1\}) + [44.9 - 6.55\log(\max\{30, H_1\})]\log(d) - a(h_v) - b(H_1) \quad (2)$$

In case of suburban environment,

$$PL_{Suburban}(dB) = PL_{Urban} - 2\{\log[(\min\{\max\{150, f\}, 2000\})/28]\}^2 - 5.4 \quad (3)$$

In case of rural environment,

$$PL_{Rural}(dB) = PL_{Urban} - 4.78\{\log[\min\{\max\{150, f\}, 2000\}]\}^2 + 18.33\log[\min\{\max\{150, f\}, 2000\}] - 40.94 \quad (4)$$

where,

$$a(h_v) = (1.1\log(f) - 0.7)\min\{10, h_v\} - (1.56\log(f) - 0.8) + \max\left\{0, 20\log\left(\frac{h_v}{10}\right)\right\} \quad (5)$$

$$b(H_1) = \min\left\{0, 20\log\left(\frac{H_1}{30}\right)\right\} \quad (6)$$

where, f is frequency in MHz, d is distance between a transmitting antenna and receiving antenna in km, H_1 is the

transmitting antenna height above the ground level in meter, h_v is the receiving antenna height above the ground level in meter. $a(h_v)$ is the correction factor of the receiving antenna height. $b(H_1)$ is the correction factor of the transmitting antenna height.

The long term fading has different variation values due to separated distance between a transmitter and receiver in urban, suburban, and rural environment. Shadow fading calls for the long term fading or the slow fading, because channel characteristics vary slowly and location between a transmitter

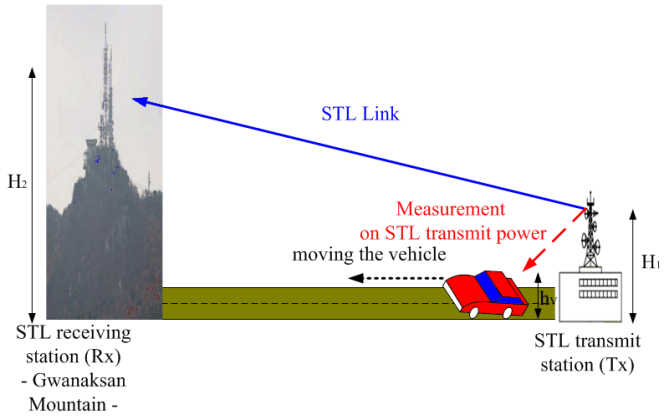

Fig. 6. Measurement method [4].

and receiver. The standard deviation of the long term fading to the separation between a transmitting antenna and receiving antenna with the distance range from 0.1 to 0.2km is 17 dB in the roof below. For the distance range of 0.2km to 0.6km, the standard deviation is s.t.d = 17-20(d-0.2)dB. For the separation distance range larger than 0.6km, there is 9dB [2], [4].

B. Results Comparison

Measurement was performed on the road in the large city including huge or small buildings and hills with moving car from STL transmit station as shown in Figure 6. The received signal strength intensity (RSSI) of SBS or FEBC STL measured to the measurement system within the car show in Figure 7 and Figure 8, relatively. Figure 7 shows on the RSSI results of SBS and Figure 8 shows on the RSSI results of FEBC on both measurement and theoretical Extended Hata pathloss. We used the received antenna of omni directional type. The height of the received omni antenna on the top of roof is 2.5m on the ground level. In Figure 7 and Figure 8, x-axis means the separated distance in a straight line between the STL transmitting antenna and received antenna. The maximum separated distacne of FEBC and SBS is 10 and 12.4km, respectively. But, the height of STL antenna on ground level is enough high to install on the tower on Mt. Gwanaksan. RSSI level is measured by enough distance to be able to approach near to the tower on Mt. Gwanaksan. For Figure 7 and Figure 8, the maximum measurement distance of FEBC is about 7 km out of 10km, and SBS is about 8.2km out of 12.4 km. As shown in Figure 4 and Figure 5, the measurement region 1 in Link 1 path and measurement region 2 in Link 2 path are the area moving the car from the STL transmitter to the front of Mt. Gwanaksan in order to measure the RSSI level, respectively. The RSSI level according to

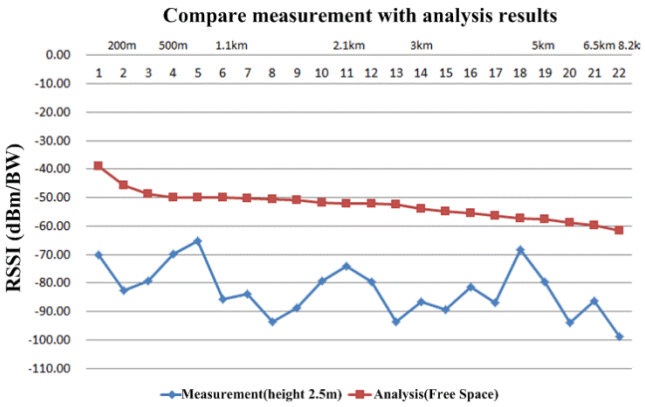

(a) measurement vs. free space model

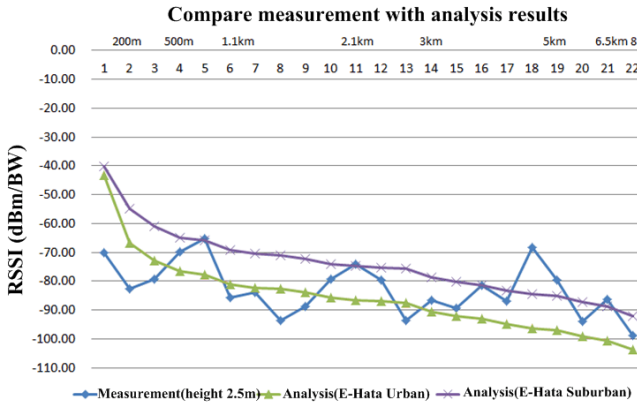

(b) measurement vs. Extended Hata model

Fig. 7. Comparison on measurement and analysis results(SBS's RSSI in the large city).

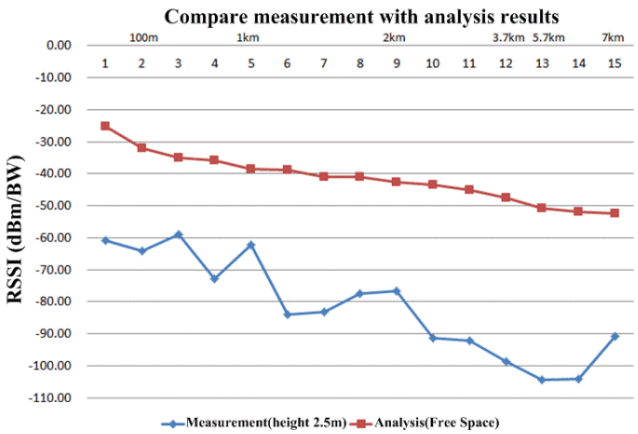

(a) measurement vs. free space model

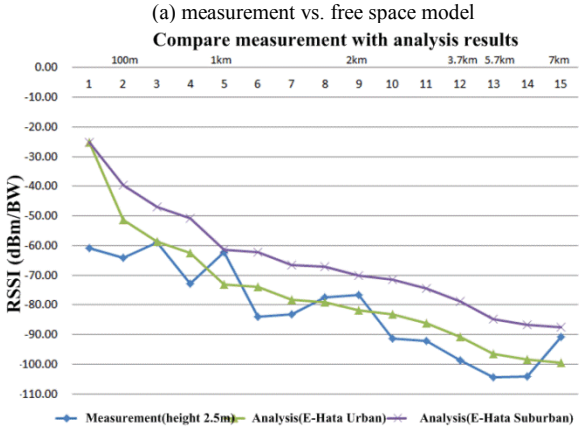

(b) measurement vs. Extended Hata model

Fig. 8. Comparison on measurement and analysis results (FEBC's RSSI in the large city).

separated distance from a transmitter and receiver varied due to the around environment including multiple buildings, many cars, and the park etc.

Figure 7 and Figure 8 show different RSSI characteristics according to distance considering the car moving path. The reduction of RSSI level according to the distance means pathloss value including the long term fading. Figure 7(a) shows that results of both measurement and the free space pathloss are compared each other.

The RSSI values to receiving antenna with the antenna height of 2.5m from the SBS transmit station with the antenna height of 70m in the urban area are -70 ~ -100dBm in the measurement results and -40 ~ -60dBm in the free space pathlss results. Figure 8(a) shows that measurement and Extended Hata (urban, suburban) pathloss results are compared each other. The RSSI values to receiving antenna with the antenna height of 2.5m from the FEBC transmit station with the antenna height of 35m in the urban area are -60 ~ -100dBm in the measurement results and -25 ~ -52dBm in the free space pathlss results. Figure 7 and Figure 8 show the long term fading characteristics.

Approximately, the fluctuation value is 10 ~ 13dB in SBS and is 6 ~ 10dB in FEBC from the STL transmit station to the Mt. Gwanaksan path. The standard deviation of shadowing in COST231 model [2] provides 3 ~ 4dB ranges. In COST231, the value has smaller variation than measurement results in the large city including the urban and suburban environment. This difference is due to the radio propagated environment including the reflection and diffraction at the buildings, obstructs, and forest etc. As shown in Figure 7 and Figure 8, the measurement results of pathloss according to the separated distance are good mapping with Extended Hata urban and Extended Hata suburban pathloss except for the measurement point of the near location from pointing station as a transmitter, although relative shadowing variation is larger than reference COST231 value of 3 ~4dB. Finally, the median pathloss is able to apply for estimating the reduction characteristics of the signal power in addition to high variation of the shadow fading with log-normal distribution in the case of the large city at 1.7GHz bands.

C. *Interference Calculation*

As shown in Figure 1, the interfering STL transmit signal cause the potential interference impact to the LTE base station reception at the frequency of 1.7GHz bands. LTE is assumed as the reverse FDD system. To calculate the interfering STL signal strength intensity and desired LTE received signal strength intensity to the LTE reception, let us consider the theoretic median pathloss and shadowing characteristics as shown in Figure 7 and Figure 8, because the interfering and wanted transmitter power are reduced according to the separated distance between the transmitter and receiver. We found facts that the median pathloss and long term fading characteristic is applied to estimate different attenuation characteristics according to the separated distance between the interfering transmitter of the fixed pointing station and the reception of the mobile communication station such as LTE system in the large city as shown in Figure 7 and Figure 8.

Figure 9 shows the interference analysis scenario to the LTE reception due to the interfering STL transmit station

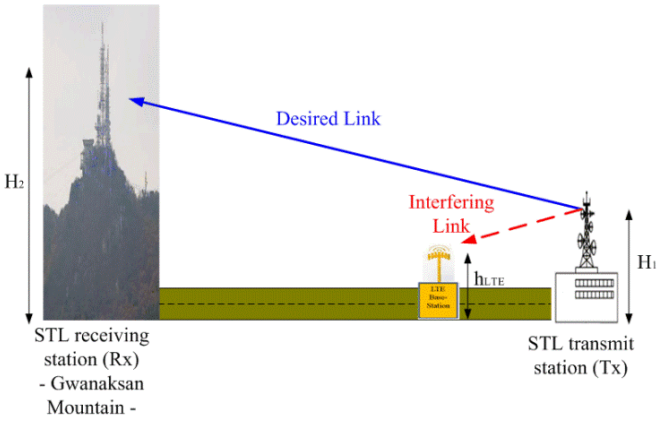

Fig. 9. Desired and interfered link [4].

when the LTE base station is located in straight line between STL links (Link 1 and Link 2) as shown in Figure 4 and Figure 5, respectively. For the calculation of the interference impacts between different systems such as the LTE receiver and STL transmitter in this paper, we used the measurement results at 1.7GHz bands in the large city shown in Figure 7 and Figure 8. Measurement was performed on the road using the receiver with the antenna height of 2.5m of the omni directional antenna type. The measurement results are calibrated on the receiving antenna height because the antenna height of receiver in the measurement is 2.5m, while the antenna height of the LTE base station is 15m. Therefore, the correction value due to difference of the receiver antenna height between 2.5m in the car and 15m in the LTE base station is required. We used the correction value of about 11dB based on the measurement according to the receiver antenna height difference.

We derived the interfering received signal strength intensity to the LTE base station reception from the emission power of the STL transmit station in the adjacent channel usage. The emission power of the STL transmits station means the totally interfering signal power received to the LTE base station receiver to the out of band spectrum of STL transmit station.

Figure 10 shows the emission characteristic of the FEBC station and Figure 11 shows the emission characteristic of the SBS station based on the realistic conducted power measurement. Equation (7) is derived to calculate the interfering received signal strength intensity to the LTE base station reception [4].

$$iRSSI\,(\mathrm{dBm}) = I_{\mathrm{ooB},\Delta F} + G_{\mathrm{Rx}}(H_1, h_{\mathrm{LTE}}, \delta) + \mathrm{a}(h_{\mathrm{LTE}}) \quad (7)$$

where, *iRSSI* depicts the totally received interfering signal strength intensity including the antenna gain and correction value $\mathrm{a}(h_{\mathrm{LTE}})$ in dB as the difference of the received signal strength intensity due to the difference of between 2.5m and 15m of the received antenna height, $I_{\mathrm{ooB},\Delta F}$ means the received interfering signal strength intensity to the reception of the LTE base station based on the measurement results as shown in Figure 7 and Figure 8. As shown in Figure 10 and Figure 11, the out of band (ooB) emission power of the fixed STL transmit station is potentially influenced to the system performance to the reception of the LTE station. The totally

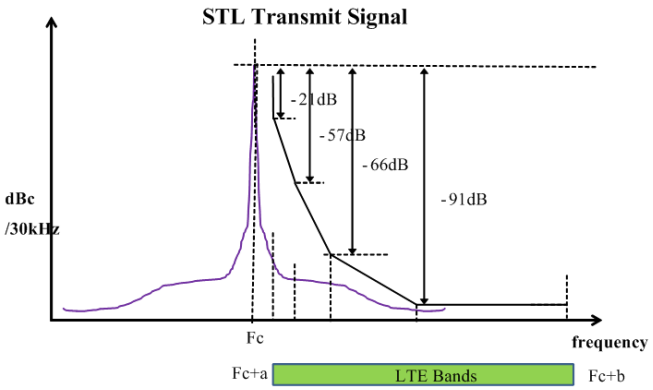

Fig. 10. FEBC Station's Emission Characteristics [4].

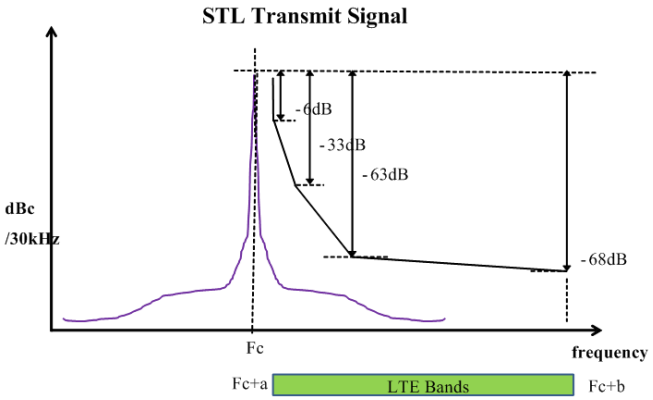

Fig. 11. SBS Station's Emission Characteristics [4].

emission power is calculated as the total transmit power received within the separation frequency (ΔF) bands from the offset (Fc+a) frequency to the end frequency (Fc+b) of the channel bandwidth of 5MHz of the LTE base station.

$G_{\mathrm{Rx}}(H_1, h_{\mathrm{LTE}}, \delta)$ depicts the total antenna gain of the LTE base station including both the antenna height of the STL transmitter and LTE base station with the antenna up or down tilting. For example, we assumed that the LTE base station has the down tilt of 3dB, the antenna end of the STL transmit station is pointed to the end of the STL receiving station. Also, the antenna gain considers the direction of the elevation angle to derive the total antenna gain. For predicting on the interference impact to the LTE base station reception, we must define the permissible totally received interfering signal strength intensity to the victim station. In this paper, a permissible interference limit is -108dBm/5MHz to the victim system as the LTE base station. This value is derived from the protection ratio of LTE base station. LTE protection ratio is I/N, which the ratio the totally received interfering signal strength intensity to noise power of the victim station such as the LTE base station [8]-[9]. The protection ratio of I/N is defined as - 6dB. This means that the permissible totally received interfering signal strength intensity to the reception must be less than the total noise power. Total noise power is derived as the equation (8).

$$N\,(\mathrm{dBm}) = 10\log(kT \cdot B \cdot NF) \tag{8}$$

where, kT depicts boltzmann constant of k and ambient temperature of T. This kT value is about -170dBm/Hz in the general communication system. B is the bandwidth of 5MHz

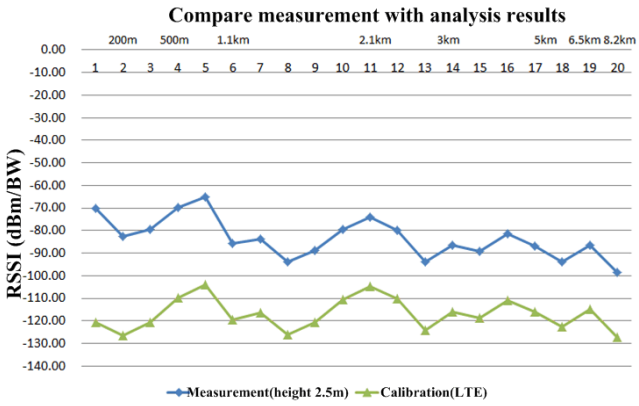

Fig. 12. SBS Station's iRSSI.

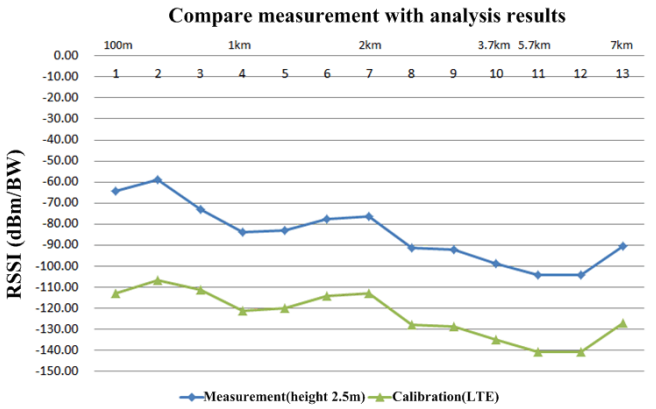

Fig. 13. FEBC Station's iRSSI.

of LTE base station and NF depicts the noise figure of 5dB of LTE base station receiver.

Therefore, the permissible totally received interfering signal strength intensity to the victim station is -114dBm/5MHz. Figure 12 and Figure 13 show the totally received interfering STL (SBS in Figure 12 and FEBC in Figure 13, respectively) signal strength intensity to the LTE base station when the receiving antenna height of the roof top to the measurement vehicular is 2.5m and the receiving antenna height of the LTE base station 15m, respectively. To limit the received interfering signal strength intensity, the separation distance is required between the STL transmit station as the interfering transmitter and the LTE base station as the victim station. If the permissible totally received interfering signal strength intensity to the reception is -114dBm/5MHz, the satisfied distance between the SBS station and LTE base station is 2.2km over in Figure 12 and the satisficed distance between the FEBC station and LTE base station is 2km over in Figure 13.

V. Conclusion

This paper described to derive composite median path loss and shadowing value for the protection of the LTE base station from the interference impact due to STL transmitter. As an approach, we measured the STL's transmission power during moving with a vehicular from the STL's broadcast studio to the STL receiver in another location. As the fixed STL microwave broadcasters, we considered two STL stations with different link paths in the large city. One STL station is FEBC and, while the other is SBS. Finally, we found to should be used the composite median pathloss with long term fading corresponding to the various urban and suburban

environments in the large area. Measurement results are in good match with the results of composite different median path loss. In addition, to calculate the interfering STL signal strength intensity and desired LTE received signal strength intensity to the LTE reception, we considered the theoretic median pathloss and shadowing characteristics. For predicting the interference impact to the LTE base station reception, we defined the permissible totally received interfering signal strength intensity to the victim station. If the permissible totally received interfering signal strength intensity to the reception is -114dBm/5MHz, the satisficed distance between the SBS transmit station and the LTE base station is 2.2km over and the satisficed distance between FEBC transmit station and the LTE base station is 2km over.

For the coexistence between the STL station and LTE base station, it is expected to use the required minimum separation distance. And, the antenna correction factor is very important value to predict the radio propagation phenomenon such as the pathloss and shadowing for high accuracy and is available to calculate the interference impact in the adjacent channel bands.

ACKNOWLEDGMENT

This work was supported by the ICT R&D program of MSIP/KCA. [2013-005-036-001, Wireless Channel and Frequency Characterization based on Field Measurements for Broadband Mobile Hot-Spot Applications]

REFERENCES

[1] S. Tomazic and G. Jakus, "Long Term Evolution: towards 4th generation of mobile telephony and beyond," in Proc. 9th Telecommunication in Modem Satellite, Cable, and Pointing Services 2009, Oct. 2009, pp.91~96.
[2] Monte-carlo simulation methodology for the use in sharing and compatibility studies between different radio services or station, European Conference of Postal and Telecommunications Administration (CEPT), ERC Report 68, Jun. 2002.
[3] Method for point-to-area predictions for terrestrial services in the frequency range 30 MHz to 3 000 MHz, ITU Radio Communication Sector(ITU-R), REC. ITU-R P.1546, Oct. 2009.
[4] Y. Yoon, J. Kim, M. Jung, and Y. Chong, "Radio propagation characteristics in the large city," in Proc. 16th International Conference on Advanced Communication Technology 2014, vol.1, no.1, Feb. 2014, pp.558-562.
[5] Telecommunication chapter I—Federal Communications Commission subchapter C—part 73—broadcast radio services, CFR Title 47, Federal Communications Commission (FCC).
[6] http://www.tftinc.com/stlproducts.html.
[7] http://www.moseleysb.com/mb/starlink_family.html.
[8] Long Term Evolution (LTE): a technical overview, Motorola, 2007.
[9] Derivation of a block edge mask (BEM) for terminal stations in the 2.6GHz frequency bands (2055-2690MHz), European Conference of Postal and Telecommunications Administration (CEPT),ECC Report 131, Feb. 2009.
[10] Y. Shim, I. Lee, and S. Park, "The impact of LTE UE on audio devices," Electronics and Telecommunication Research Institute Journal, vol.35, no.2, Apr. 2013, pp.332-335.

YoungKeun Yoon received B.S, M.S, and PhD degrees in radio engineering from National Chungbuk University, Korea, in 1997, 1999, and 2007, respectively. Since 2000, he has been working Electronics and Telecommunications Research Institute (ETRI). He has been involved in the research of radio resource management and propagation since 2003. His main interests are radio propagation and spectrum engineering study in indoor and outdoor environments

JongHo Kim received B.S, M.S, and PhD degrees in electronic engineering from Chungnam National University, Daejeon, Korea, in 1986, 1988, and 2006, respectively. Since 1989, he has been working for ETRI, Daejeon, Korea, where he is a principal member of the engineering staff of the Radio Technology Department. His main interests are radio propagation and spectrum engineering.

MyoungWon Jung received B.S, M.S, and PhD degrees in electronic engineering from Chungnam National University, Korea, in 2006, 2008, and 2014, respectively. Since 2009, he has been working for ETRI, where he is a senior member of research staff of the radio technology department. His main interests are radio propagation study for mobile communication and millimeter wave propagation study in indoor and outdoor environments.

YoungJun Chong received the B.S degree from the Jeju University, Jeju island, Korea, in 1992, and the M.S degree in electronics engineering in 1994 from Sogang University, PhD degree in electronic engineering from Chungnam National University, Korea, in 2005, respectively. Since 1994, he has been with ETRI, Korea, where he is a leader of spectrum engineering section and principle member of the research staff of the radio technology department. He is currently involved in the development of the digital ultra-narrow band walky-talky. His research interests include RF circuit and stations development

Vertical Handoff Decision Algorithm in Heterogeneous Wireless Network Based on Queuing Theory

Yong Sun*,**

*Beijing Key Laboratory of Network System Architecture and Convergence

**Beijing University of Posts and Telecommunications, Beijing, China 100876

sunyong@bupt.edu.cn

Abstract— **A smart vertical handoff decision algorithm based on queuing theory is proposed in this paper. Vertical handoff in heterogeneous wireless network is crucial to the future wireless communication. The algorithm formulates the heterogeneous wireless area and handoff procedure using queuing theory and proposes a new network selection index called new handoff blocking probability to evaluate the network performance. A RSS-based mechanism is considered to avoid the Ping-Pong effect. Also the network architecture is regulated to manage the wireless resource effectively. The experimental results show that the proposed algorithm outperforms the traditional algorithm with low handoff blocking probability and a better load balance of the whole wireless environment.**

Keyword—**Heterogeneous wireless networks, Queuing theory, Wireless resource management, Vertical handoff**

I. INTRODUCTION

With the rapid development of wireless technologies, the evolution of mobile communication result in an increasing number of heterogeneous networks. The future wireless networks are imaged as a combination of multiple wireless access networks like WIFI, WiMAX, Universal Mobile Telecommunications System (UMTS) and LTE, which can provide mobile users with Always Best Connected (ABC) services [1]. Mobile users will more likely face the environment in which a number of wireless networks coexist for a long period of time [2]. So it is crucial to integrate heterogeneous networks and offer mobile users better services. In such wireless network environment, the universal seamless handoff between heterogeneous wireless technologies is a challenging problem. Facing this problem, the architecture for 4th Generation (4G) wireless networks aims to integrate various heterogeneous wireless access networks over an IP backbone [3].

In heterogeneous wireless networks, handoff can be divided into two categories: horizontal handoff (HHO) and vertical handoff (VHO) [5].A HHO is made among different access networks when changing a connection from one access point (AP) to another or one base station (BS) to another, that is to say, the network have the same link-layer technology. While a vertical handoff happens between access networks with different link-layer technologies, such as changing a connection between an AP and a BS. Compared with the horizontal handoff, the vertical handoff is more complex for application. One of the main challenges for vertical handoff is how the handoff strategy determines the "best" network from the available heterogeneous candidate networks [4]. In this way handing off to a different network can be regarded as a multiple attribute decision making (MADM) problem. And in the progress of MADM, it is necessary to estimate the weights of the factors comprehensively, so as to make a good trade-off between the performance optimization of single MN and efficient utilization of whole wireless environment.

The rest of the paper is organized as follows: we briefly review the related works about vertical handoff decision algorithms In Section II. In Section III, a vertical handoff decision algorithm based on queuing theory is proposed. Then Section IV shows the performance evaluation of our proposed algorithm. Finally, a conclusion is summarized in Section V.

II. RELATED WORK

The received signal strength (RSS) is usually used in traditional vertical handoff algorithms. MADM is a popular method to select a target network from a set of candidate networks that have many attributes to consider. Some of MADM methods are: 1) SAW (Simple Additive Weighting); 2) TOPSIS (Technique for Order Preference by Similarity to Ideal Solution); 3) AHP (Analytic Hierarchy Process); 4) GRA (Grey Relation Analysis) [6]. Then some other handoff algorithms are proposed and can be summarized as following. (1) Fuzzy logic, fuzzy logic is proposed to represent the imprecise information of the conditions about the heterogeneous networks and to adapt dynamically to evaluate multiple attributes simultaneously [7]. (2) AHP (Analytic Hierarchy Process), AHP decomposes the network selection problem into several sub-problems and assigns a weight value

Manuscript received October 6, 2014. This work was supported in part by the National Natural Science Foundation of China under Grant 61101106, by the Fundamental Research Funds for the Central Universities under Grant 2013RC0120, 2011RC0107

Y. Sun is with the School of information and communication engineering, Beijing University of Posts and Telecommunications, Beijing, China 100876, and Beijing Key Laboratory of Network System Architecture and Convergence (corresponding author: +86-131-4131-8816; fax: +86-10-6228-3279; e-mail: sunyong@bupt.edu cn).

to each sub-problem [8]. Then, the network with the highest performance score is selected. (3) SSF (Strongest Signal First), in this model RSS is the only affecting factor of selecting access network.

Although various vertical handoff algorithms are proposed, some problems remain unsolved. Some algorithms, such as SSF, tend to adopt a simple decision algorithm to maintain a faster handoff procedure. But the simple decision-making mechanism may not help to select a suitable network and may also yield serious Ping-Pong effect. Others regard the handoff decision procedure as a multiple attribute decision making problem [9-11, 16] and tend to solve the problem by searching for the optimal solution. These algorithms emphasize on the optimized network for single MN (mobile node) and neglect the evaluation of the whole wireless environment, which may cause the unbalanced loads distribution, serious time delay and the increasing number of handoff dropping. To overcome these problems, our algorithm is proposed. In this paper we formulate the whole heterogeneous wireless environment and handoff procedure using queuing theory. And a RSS-based mechanism is considered to avoid the Ping-Pong effect. We also regulate the network architecture to manage the wireless resource effectively. Then, we propose a new network selection index called new handoff blocking probability to evaluate the network performance. Finally a smart vertical handoff decision algorithm based on queuing theory is proposed.

III. The Proposed Scheme

In heterogeneous wireless networks, the coverage environment can be divided into two areas: cellular coverage area and WLAN hotspots area. The WLANs are typically configured as small cells within the "cellular coverage area" of GPRS/UMTS or LTE, which is relatively larger compared with WLAN hotpots [12]. The cellular coverage area is covered by a set of overlapping BSs $B=\{b_1,b_2\cdots b_M\}$ and a set of WLAN APs $A=\{a_1,a_2\cdots a_N\}$. In our algorithm, the cellular coverage area is implemented in a vertical handoff decision system (VHDS). The VHDS consists of two parts: multiple vertical handoff decision transducers (VHDT) and a central vertical handoff decision controller (CVHDC). VHDTs are located in each access network in order to provide real-time network conditions and handoff requests of networks in the cellular area. CVHDC execute the vertical handoff decision for the whole wireless region after analyzing the collected message from VHDTs. The signaling interaction between CVHDC, VHDT and access networks will be obtainable by the media independent handoff (MIH) which is defined in IEEE 802.21 [13].

VHDS maintains the sets A and B which covers the cellular coverage region as a list S of candidate access points. All available WLAN APs in set A and BS in set B are added into S. In addition, we define $U=\{u_1,u_2\cdots u_K\}$ as the set of all the mobile nodes (MN) which have the probability to access the network in the cellular coverage region. Only these K MNs are considered in this model and each MN is either requesting a handoff (or just turned on and require channel) or remains connected to an AP ($\in A$) or BS ($\in B$). Then, we divide the set U into two subsets at a certain time: $U_h(t)$ and $U_r(t)$.

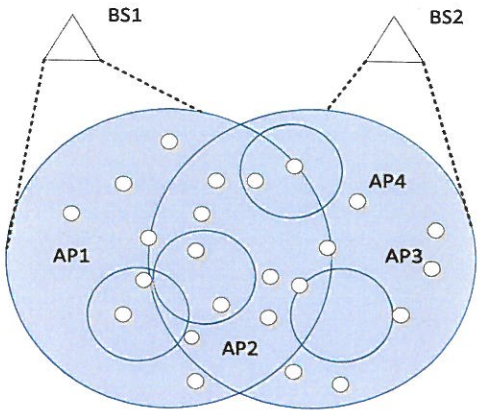

Figure.1. simulation topologies of heterogeneous networks

$$U_h(t)=\{u_{h1},u_{h2}\cdots u_{h(t)}\} \quad (1)$$

In equation (1), $U_h(t)$ stands for the set of MNs which request handoff at the certain time t and $h(t)$ is the number of set $U_h(t)$.

$$U_r(t)=U-U_h(t)=\{u_{r1},u_{r2}\cdots u_{r(t)}\} \quad (2)$$

Accordingly, $U_r(t)$ is the complementary set of $U_h(t)$ and represents the MNs which will remain the connection to the current networks at the certain time. $r(t)$ is the number of set $U_r(t)$.

In this scene, the bandwidth change problem can be formulated by queuing theory. It is noted that the vertical handoff decision algorithm is deployed in each AP or BS. And each AP or BS has the limitation to the available bandwidth which means that the channels provided by the network is limited by each network and only certain number of connection can be maintained. To simplify the problem, we assume that only La channels and Lb channels are allocated by each AP or BS respectively. Fig.1 shows the decision-making epochs of CVHDC.

The sequence $T=\{t_1,t_2\cdots t_z\}$ represents successive time epochs, where the variable t_z denotes the current time epoch. For each network i, the handoff arrival rate sequence $X_i=\{x^i_1,x^i_2\cdots x^i_{z-1}\}$ and the service complete rate sequence $Y_i=\{y^i_1,y^i_2\cdots y^i_{z-1}\}$ will be stored and CVHDC will make the decision at t_z based on them.

For the traffic characteristics, the handoff decision and channel allocation process of a network a_i or b_i can be formulated as $M/M/n/n$ model. To dynamically adjust the process of network selection, we make the variable n dynamically respect the available channels $La_{(av)}$ and $Lb_{(av)}$ which are not occupied by MNs for AP and BS, respectively. The arrival of handoff requests for channels follows a Poisson distribution with mean λ_i and the service holding time is assumed in a negative exponential distribution with mean $1/\mu_i$ for each network i. These assumptions are common in the many researchers [14, 15]. However, in our model we will dynamically adjust the λ_i and μ_i according to the real-time network condition sequences X_i and Y_i which is

Figure 2 Successive time epochs of network

stored in CVHDC. So λ_i and μ_i will change in each time epoch and can be redefined to $\lambda_i(t_{z-1})$ and $\mu_i(t_{z-1})$ as function (3) and (4).

$$\lambda_i(t_{z-1}) = (1/t_{z-1})\sum_{k=1}^{z-1} x_k \tag{3}$$

$$\mu_i(t_{z-1}) = (1/t_{z-1})\sum_{k=1}^{z-1} y_k \tag{4}$$

The network in the cellular coverage area does not have holding queue, so the handoff will be blocked if all n channels of target network is occupied. Thus, we can define the probability which the network i is fully occupied as the new handoff blocking probability (NHBP) P_i which is derived from the new call blocking probability. P_i is defined according to the queuing theory as function (5). And we also propose the max blocking probability of the entire area by function (6).

$$P_i = (\lambda_i(t_{z-1})/\mu_i(t_{z-1}))^n (n!\sum_{j=0}^{n}((\lambda_i(t_{z-1})/\mu_i(t_{z-1}))^j/j!))^{-1} \tag{5}$$

$$P_b = MAX_{1\le i\le M+N}(P_i(E)) \tag{6}$$

The variable P_b is the max blocking probability of the entire cellular coverage area before the CVHDC makes the handoff decision at t_z. And our algorithm is aiming at minimizing the max blocking probability of the entire cellular coverage area.

To describe the connection status between MNs ($\in U$) and networks ($\in A \bigcup B$), a matrix $C(t) = \{c_{ij}\}_{(M+N)\times K}$ for the cellular coverage area is proposed. c_{ij} is equal to 1 only when there is a connection between network a_i or b_i and the MN u_j and 0 otherwise.

We also define the possible association matrix at t_z as $C'(t_z) = \{c'_{ij}\}_{(M+N)\times K}$:

$$c'_{ij} = \{0,1\} \tag{7}$$

$$c'_{ij} = 0 \quad RSS_{ij} < \begin{cases} \theta_a & \text{for } 1 \le i \le N \\ \theta_b & \text{for } N+1 \le i \le N+M \end{cases} \tag{8}$$

$$\sum_{i=1}^{N+M} c'_{ij} = 1 \tag{9}$$

In the possible association matrix $C'(t_z)$, c'_{ij} is defined as 1 in two situations. One is that the MN u_j remains connected to the current network a_i or b_i. Another is that the MN u_j will hands off to the candidate network a_i or b_i. Each MN in the set $U_h(t)$ may have multiple candidate networks which satisfy the RSS thresholds θ_a (for AP) or θ_b (for BS), so the possible association matrix may also be multiple. Accordingly, we define $\chi(t_z)$ as the set of possible

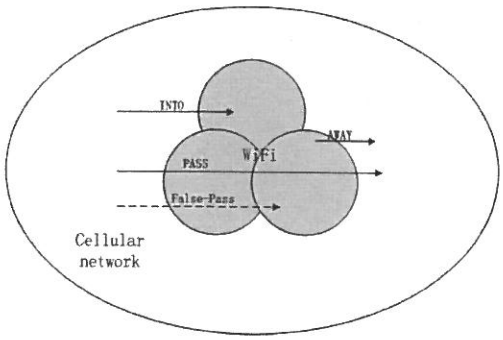

Figure 3 Handover modes

association matrices of t_z. For each possible association matrix $C'(t_z)$ in $\chi(t_z)$, we will generate a handoff matrix by the function (10):

$$H(t_z) = C'(t_z) - C(t_z) = \{H_{ij}\}_{(M+N)\times K} \tag{10}$$

$H(t_z)$ denotes the originate network i and the target network j of the handoff of MN u_k with the value $h_{ik} = -1$ and $h_{jk} = 1$. $h_{\alpha\beta}$ is equal to 0 only when the MN u_β remains the current connection. For the certain network i, we calculate the number of -1 and 1 in the i row of $H(t_z)$ as x_{off} and x_{in}, which denotes the number of MNs leaving and accessing the network. Then the model can be reformulated as following. For each network i:

$$\lambda_i(t_z) = (1/t_z)(\sum_{k=1}^{z-1} x_k + x_{in}) \tag{11}$$

$$\mu_i(t_z) = (1/t_z)(\sum_{k=1}^{z-1} y_k + x_{off}) \tag{12}$$

$$P_i(\mathrm{E}) = (\lambda_i(t_z)/\mu_i(t_z))^n (n!\sum_{j=0}^{n}((\lambda_i(t_z)/\mu_i(t_z))^j/j!))^{-1} \tag{13}$$

And for any possible association matrix $C'(t_z) \in \chi(t_z)$,

$$P_b(C'(t_z)) = MAX_{1\le i\le M+N}(P_i(E)) \tag{14}$$

Thus an algorithm aimed at minimizing expected new handoff blocking probability is proposed as follows:

$$\text{Min-P: } Min_{\forall C'(t_z)\in\chi(t_z)}(MAX_{1\le i\le M+N}(P_i(E))) \tag{15}$$

To avoid the Ping-Pong effect, a RSS-based mechanism is considered. We give four following modes to describe the movement of MN in Fig. 3. INTO mode: MN moves into some WLAN network from cellular network. AWAY mode: MN moves away from WLAN to cellular network. PASS mode: MN moves through WLAN networks from cellular network to the same cellular network in short time. False-Pass mode: MN moves into WLAN at a high speed, then moves at a low speed even stays in WLAN It is the supplement of PASS mode.

In the proposed algorithm, when MN is connecting to WLAN, MN detects RSS of the around APs to select the best AP. We use the generally applied radio communication model [9], defined as:

$$\text{RSS}=P_0\text{-}32.44\text{-}20\lg f_c\text{-}20\lg d\text{-ShadowFading+FastFading} \tag{16}$$

Where P_0 (dBm) is the transmitting power of BS or AP, f_c (MHz) is the carrier frequency and d (km) is the distance from MN to BS or AP.

IV. Simulation Results And Analysis

In this section, our algorithm is evaluated by simulation compared with the AHP algorithm and SSF (Strong-Signal First). To ease our illustration, we just consider the situation in which there are two kinds of networks 3G and 802.11b. And the above two integrated heterogeneous wireless networks represent the set B and the set A in our algorithm respectively. The simulation topologies of heterogeneous wireless networks are shown in Fig.1. The cellular coverage area is covered by two overlapping 3G BSs and four 802.11b hotpots. The maximum bandwidth of BSs and APs are predefined as 3mbps and 7 mbps, respectively. Besides, the bandwidth requested by each MN is constant 0.2mbps. So according to the service request of MN, we can divide the BS and AP in 15 and 35 Channels. Then the model can be formulated as *M/M/35/35* and *M/M/15/15* for each BS and AP.

At the beginning of the simulation, MNs are evenly distributed over the coverage area. The MNs move around during the entire simulation time. We utilize a random mobility method to characterize the movement of MNs in the coverage environment. All the attributes (including RSS) for each MN and AP or BS association are reselected after each such movement. For simplicity, it is assumed in the simulations that each BS or AP will satisfy the MN's RSS threshold if it is within the coverage area of that BS or AP.

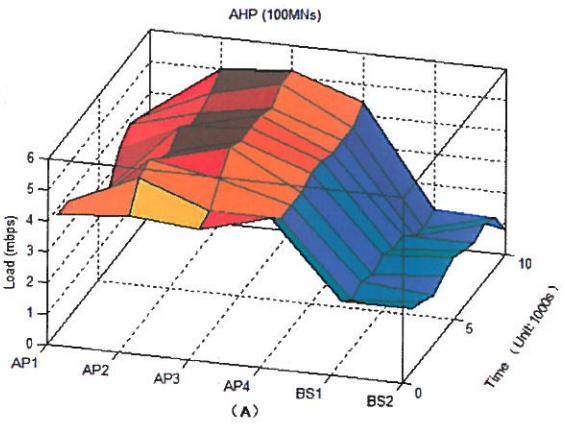

Figure 4. Load status for the AHP algorithm, when there are 100 MNs

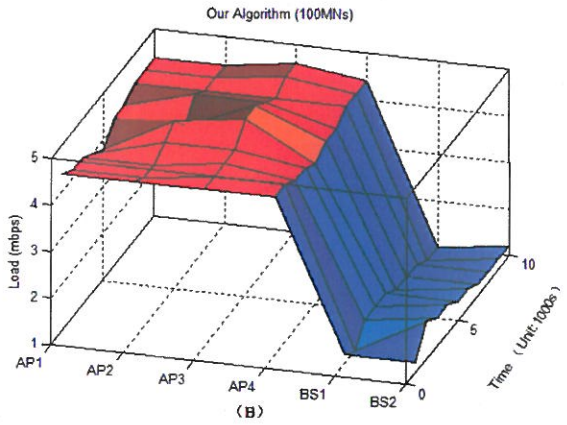

Figure 5. Load status for the our algorithm, when there are 100 MNs

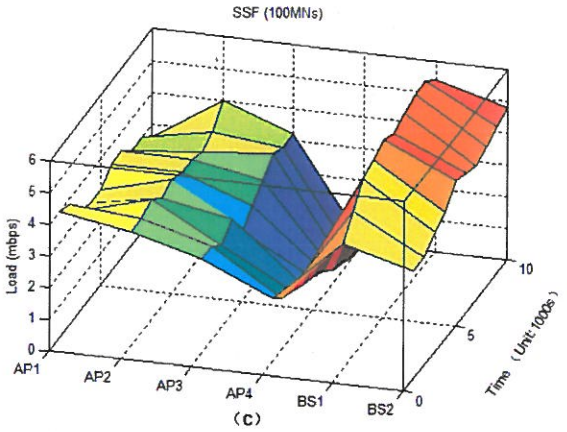

Figure 6. Load status for the SSF algorithm, when there are 100 MNs

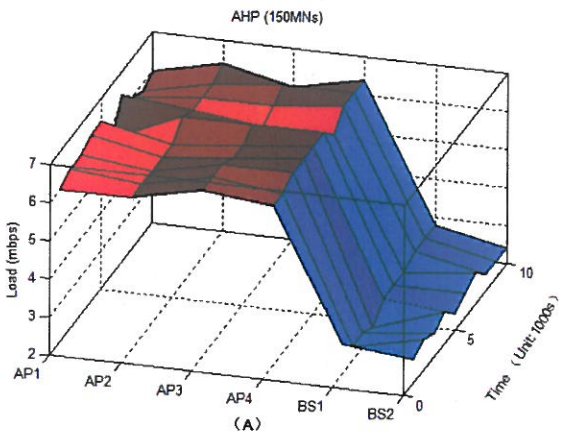

Figure 7. Load status for the AHP algorithm, when there are 150 MNs

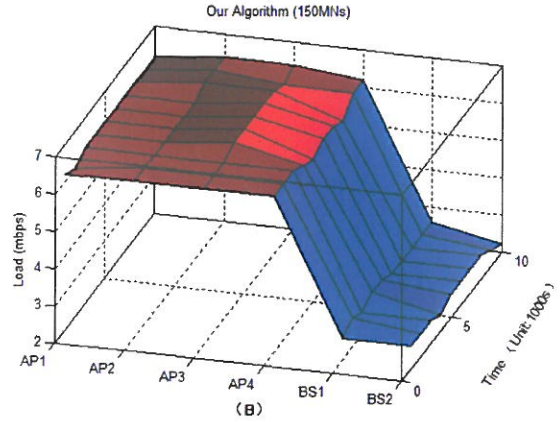

Figure.8. Load status for the Our algorithm, when there are 150 MNs

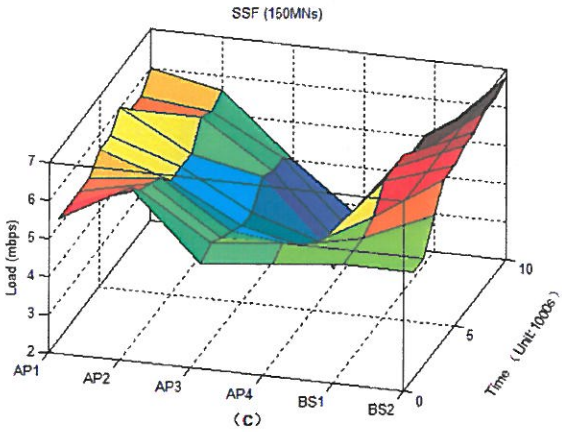

Figure 9. Load status for the SSF algorithm, when there are 150 MNs

We evaluate the load balancing performance of our algorithm, the AHP algorithm and the SSF (Strong-Signal First) method. The lower the value is the better performance of load balancing the algorithm gets. Two independent simulations run with a duration of 1000s with the number of MNs 100 and 150, respectively.

In Fig. 4 to 6, we plot the overall load at each AP and each BS versus the simulation time for the first test case with 100MNs active in the test area. Similarly, the overall loads for the second test case with 150 active MNs are plotted in Fig. 7 to 9. These figures show how the load is distributed among heterogeneous networks. In different cases, the same result occurs. Our algorithm achieves the best performance in terms of the distribution of load, the AHP algorithm comes second and the SSF method performs worst.

From Fig. 10, it is easy to find out that when the quantities of connected MNs increase, the AHP algorithm and our algorithm both get a better load balance. However, the performance of SSF may perform even worse. In all case, our method gets better performance than the AHP algorithm and the SSF method.

Fig. 11 shows the maximum of handoff dropping probability in the six candidate networks when classifying the traditional AHP algorithm and our algorithm; the quantities of MNs increase from 100 to 150. The red plots in Figures 10 correspond to the traditional AHP algorithm and the blue plots correspond to ours. It could be seen that the maximum of

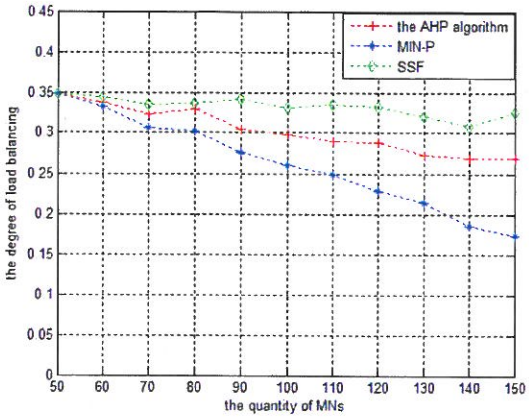

Figure 10. Load status for the SSF algorithm, when there are 150 MNs

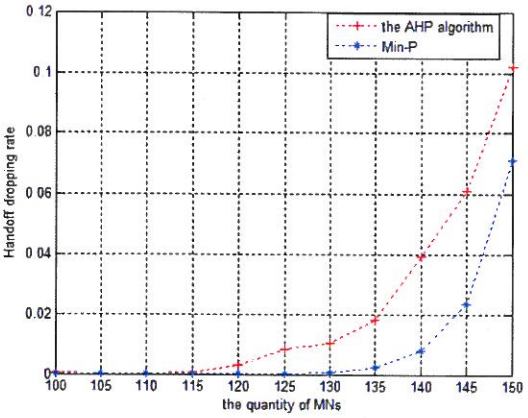

Figure.11. the maximum of handoff dropping probability in networks when MNs increase

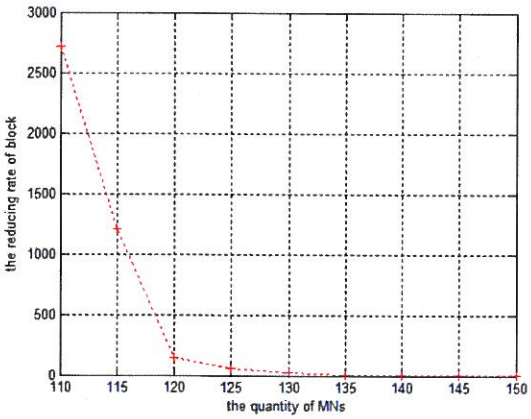

Figure 12. ratio of reducing the handoff dropping probability between the AHP algorithm and our algorithm

handoff dropping probability in the six candidate networks increases monotonically when the connected MNs of the whole simulation area increase, which comply with the real situation. And it is also visible that when the quantity of connected MNs and the loads of the simulation area vary, our method always shows the improvement of reducing the maximum of handoff dropping probability over the traditional AHP algorithm.

More specially, in Fig. 12, we can also evaluate the multiples of reducing the max handoff dropping probability the between traditional AHP algorithm and our algorithm.

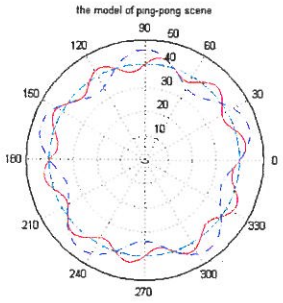

Figure 13. The simulation model of Ping-Pong scene under regular motion

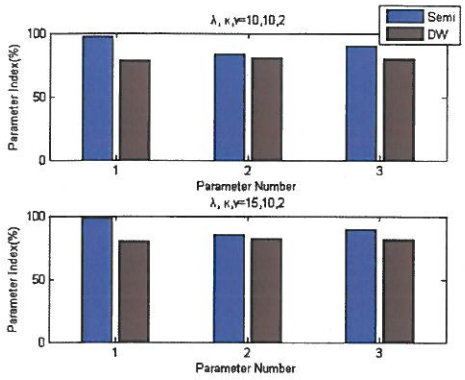

Figure 14. The simulation result1 in the Ping-Pong scene

The results show that our algorithm always outperforms the traditional AHP algorithm though the ratio of reducing handoff probability decreases sharply when the loads of the whole area increase.

Ping-Pong effect is considered in this algorithm. Ping-Pong means the interval is short between MN's continual vertical handovers. MN in this scene moves in state of Ping-Pong motion, i.e. has a to-and-fro movement in the edge of WLAN area. For simplifying, the WLAN area is assumed to have one AP. The AP's RSS is proportional to the polar coordinates equation of motion of MN, which is defined as:

$$r = 40 + \lambda \sin(k\theta) \tag{16}$$

where λ and k are trace coefficients. Fig. 13 presents the simulation model, including the motion traces in different λ and k. MN moves at constant speed according to the trace.

The model is used to evaluate the comprehensive performance of vertical handover algorithms in Ping-Pong motion, including selection of handoff time and the probability of Ping-Pong effect.

When the distance from MN to AP is not less, MN is supposed to choose WLAN, else, choose the cellular network. In that case, we say MN $\in U_h(t)$ hits the network. Hit ratios of cellular network and WLAN network are given in the simulation result to distinguish the algorithm performance into WLAN and out of WLAN.

In Fig. 14 and Fig. 15, parameter number 1 represents hit ration of WLAN, 2 is hit ratio of the cellular network, and 3 is the total hit ratio. From the results in Fig.14 and Fig.15, the performance of the proposed algorithm is higher than Dwelling-time algorithm on the whole.

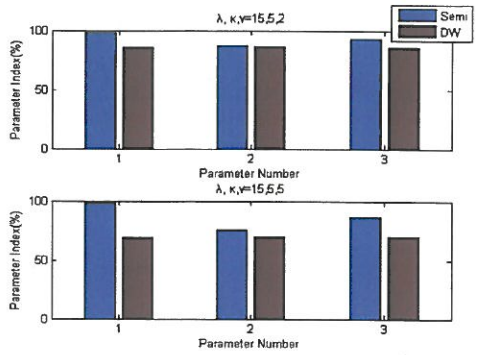

Figure 15. The simulation result2 in the Ping-Pong scene

V. Conclusion

In this paper, we focus on the metrics selection for the VHD and propose an index named new handoff blocking probability to evaluate the network performance. We also formulate the network architecture by adding VHDS (including VHDT and CVHDC) to manage wireless resources effectively. A method is used to avoid Ping-Pong effect. Then a smart vertical handoff decision algorithm is proposed based on queuing theory. The performance results based on detailed simulations show that our algorithm performs much better than the conventional AHP algorithm and SFF method. The proposed algorithm not only ensures the accuracy in network selectivity but also reaches the balance of load distribution over APs and BSs and effectively reduces the probability of handoff dropping.

Acknowledgment

Authors thank for support of the State Grid Corporation of China technology project.

References

[1] E. Gustafsson and A. Jonsson, "Always best connected",*IEEE Wireless Communication Magazine*, Vol. 10, no. 1, pp.49-55, Feb 2003.

[2] *Universal mobile telecommunications system (UMTS); evolution of 3GPP system*, ETSI TR 121 902 V9.0.0 2010.

[3] E. Stevens-Navarro, Y. Lin and V. W. S. Wong, "An MDP-based vertical handoff decision algorithm for heterogeneous wireless networks," *IEEE Transactions on Vehicular Technology*, vol.57, pp. 1243-1254, 2008.

[4] Liu, X., et al., "An improved consumer goods market model-based vertical handoff decision algorithm". *IEICE Electronics Express*, 9(4): pp. 234-239,2012.

[5] M. Liu, Z. C. Li, X. B. Guo, E. Dutkiewicz and D. Zhang, "Performance evaluation of vertical handoff decision algorithms in heterogeneous wireless networks," in *IEEE GLOBECOM '06*.2006, pp. 1-5.

[6] M. Kassar, B. Kervella and G. Pujolle, "An overview of vertical handover decision strategies in heterogeneous wireless networks," *Computer Communications*, vol.31, pp. 2607-2620, 2008.

[7] A. Calhan and C. Ceken, "An Optimum Vertical Handoff Decision Algorithm Based on Adaptive Fuzzy Logic and Genetic Algorithm," *Wireless Personal Communications*, vol.64, pp. 647-664, 2012.

[8] P. Zhang, W. Zhou, B. Xie, and J. Song, "A novel network selection mechanism in an integrated WLAN and UMTS environment using AHP and modified GRA," in *IEEE IC-NIDC*, 2010, pp. 104-109.

[9] S. F. Zhu, F. Liu, Z. Y. Chai, Y. T. Qin and J. S. Wu, "Simple harmonic oscillator immune optimization algorithm for solving vertical handoff

decision problem in heterogeneous wireless network," *Acta Physica Sinica*, vol.61, 2012..

[10] Y. S. Guo, G. Z. Tan, A. Libda and L. Q. Ma, "A QoS-aware vertical handoff algorithm based on predictive network information," *Journal Of Central South University*, vol.19, pp. 2187-2193, 2012.

[11] E. Arun and R. S. Moni, "Optimization of Vertical Handoff Decision Algorithm for Wireless Networks," *International Journal Of Computers Communications & Control*, vol.7, 2012.

[12] S. Lee, K. Sriram, K. Kim, Y. H. Kim and N. Golmie, "Vertical handoff decision algorithms for providing optimized performance in heterogeneous wireless networks," *IEEE Transactions on Vehicular Technology*, vol 58, pp. 865-881, 2009.

[13] *Standard and Metropolitan Area Networks: Media Independent Handover Services*, IEEE Std. 802.21, Jan. 2006.

[14] D. J. He, C. X. Chi, S. M. Chan, C. Chen, J. J. Bu, and M. J. Yin, "A Simple and Robust Vertical Handoff Algorithm for Heterogeneous Wireless Mobile Networks," *Wireless Personal Communications*, vol. 59, pp. 361-373, 2011.

[15] C. Oliveira, J. B. Kim and T. Suda, "Adaptive bandwidth reservation scheme for high-speed multimedia wireless networks," *IEEE Journal on Selected Areas in Communications*, vol.16, pp. 858-874, 1998.

[16] C. Gu, M. Song, Y. Zhang, L. Wang, and J. Song, "Novel network selection mechanism using AHP and enhanced GA," in *CNSR '09*.2009, pp. 397-401.

Yong Sun (M'12) received the Ph.D. degree from Beiijng University of Posts Telecommunications, Beijing, China, in 2008. He is currently a Lecturer with the School of information and communication engineering, Beiijng University of Posts Telecommunications, Beijing, China. He became a Member (M) of IEEE in 2012. His current research interests include heterogeneous networks, wireless resource allocation, and network management.

A Real-time Rectification using an Adaptive Binary Encoding for High-resolution Video

Jong-hak Kim*, Jung-kyun Oh**, Seong-muk Kang***, Jun-dong Cho***

*Department of IT convergence, Sungkyunkwan University, Korea

**Department of Human ICT convergence, Sungkyunkwan University, Korea

***Department of Electrical and Computer Engineering, Sungkyunkwan University, Korea

jhakkim@vada.skku.ac.kr, jkoh@vada.skku.ac.kr, smkang@vada.skku.ac.kr, jdcho@skku.edu

***Abstract*—Previously, various rectification methods using compressed lookup table have been studied for real-time hardware stereo vision system. These loss compression methods may occur distortion that could corrupt disparity estimation process. Differentially encoded lookup table method which is lossless compression has no distortion with reasonable compression ratio. However, the method is limited to low-resolution and low warping movement. In this paper, we propose an adaptive binary encoding method. Our proposed algorithm has approximately 10~26% compression ratio which is comparable to the previous method and tolerates high-resolution video.**

***Keyword*—real-time processing, high-resolution rectification, lookup-table, adaptive binary encoding, lossless compression**

I. INTRODUCTION

A STEREO vision system has four steps. The first step is rectification as a pre-processing. A role of rectification is to align epipolar lines. And the second step is disparity estimation to obtain disparity-map. In the third step, filtering techniques are utilized to enhance disparity-map. Finally, disparity-map is used for various applications such as visual fatigue decrease, object segmentation and tracking, motion control and etc. Since rectification not only aligns epipolar lines but also decreases search-range for disparity estimation process, it is essential process to achieve real-time processing. Figure 1 shows reduced search-range.

Rectification could categorize into real-time calculation and pre-calculation using a LUT (Lookup table). Since real-time calculation consist a large amount of computation, many research tried to simplify calculation of epipolar geometry matrix as in [2]–[4]. And a hardware architecture using FPGA (Field-programmable gate array) is also used to achieve real-time processing as in [5]–[7]. However, simplified calculation methods are not suitable for real-time processing. And FPGA methods could process in real-time, but they consist of complex hardware architecture.

On the other hand, pre-calculation using a LUT has fast processing-time with compact hardware architecture as in [8]. But disadvantage of this method is high memory consumption. To overcome this issue, loss and lossless compression techniques are applied. One of the loss compression methods subsamples rectification mapping data and reconstructs using interpolation as in [9], [10]. Although the loss compression method has much higher compression ratio than the lossless compression method, it also has distortion, and could be critical for the performance of disparity estimation process. To avoid distortion, reference [11] uses differential encoding and decoding using only subtraction and accumulation that consumes only 1.3Mbytes for a 1280 by 720 image with 27% compression ratio. Another recent research using the run-length encoding technique with different order as in [12] shows high performance. However, these methods limit data magnitude bits, so data magnitude have to be less than 3 for differential coding and 1 for run-length coding which are not suitable for high-resolution rectification.

In this paper, we propose an adaptive differential encoding method. We analysed probability of appearance of

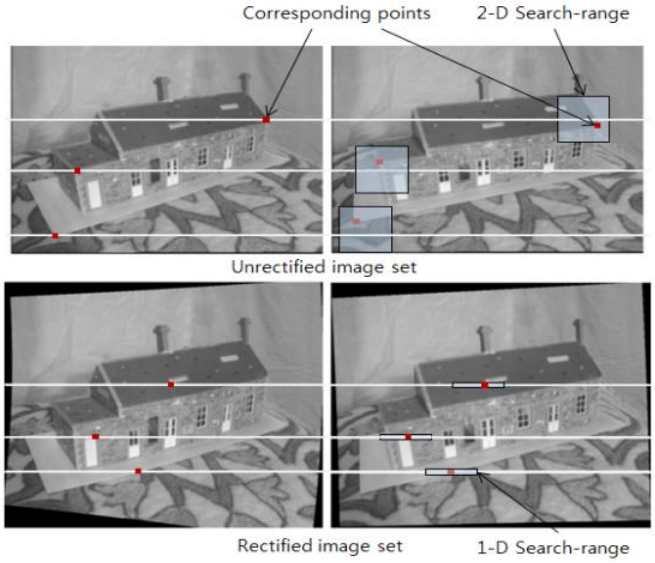

Fig. 1. Example of reduced search-range[1].

Manuscript received September 4, 2014. Followings are results of a study on the "Leaders in Industry-university Cooperation" Project, supported by the Ministry of Education, Science & Technology (MEST). This research was supported by Basic Science Research Program through the National Research Foundation of Korea(NRF) funded by the Ministry of Education(NRF-2013R1A1A2058942)

Jong-hak Kim is with the department of IT convergence, Sungkyunkwan University, Suwon, Gyeonggi-do 440-746, Korea (phone : 031-290-7200, e-mail: jhakkim@vada.skku.ac.kr).

Jung-kyun Oh is with the department of Human ICT convergence, Sungkyunkwan University, Suwon, Gyeonggi-do 440-746, Korea (e-mail: jkoh@vada.skku.ac.kr).

Seong-muk Kang and Jun-dong Cho are with the Department of Electrical and Computer Engineering, Sungkyunkwan University, Suwon, Gyeonggi-do 440-746, Korea (e-mail: smkang@vada.skku.ac.kr; jdcho@skku.edu).

differential values and built two codebooks for high performance and resolution including two and four modes. The first mode in the both codebooks is comprised of minimum bit size to decrease compression ratio, and the fourth mode in the codebook with four modes could extent bit size for magnitude to tolerate high-resolution video.

The rest of paper is organized as follows. We will introduce basic concept of rectification using LUT in Section II. Our proposed algorithm will be presented in Section III. Proposed hardware architecture will be presented in Section IV. Experimental result will be given in Section V, and finally, we will draw the conclusion in Section VI.

II. Basic Concept of Rectification using LUT

Rectification is used for various applications such as ortho-photo or ortho-image as in [13], [14], multi-view camera system as in [6], [15], intelligent vehicle using stereo vision system as in [16], [17] and etc. Difference between stereo vision system and others is that position of each camera is fixed, which needs only one set of rectification parameters if there is no individual movement of each camera and uses it consistently. Therefore, we are allowed to pre-calculate rectification mapping data and rectify images by loading mapping data from LUT memory.

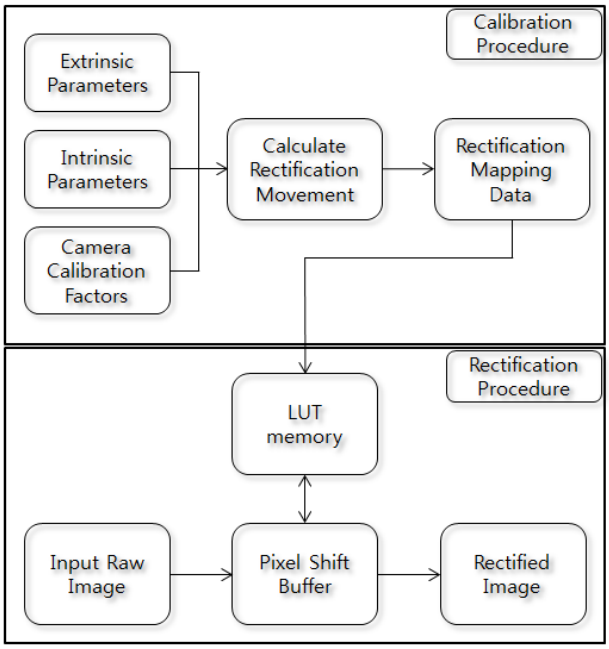

Fig. 2. Overall flow of rectification using LUT

Rectification using LUT could divide into calibration and rectification procedures. The calibration procedure is to calculate rectification movement using intrinsic parameters, extrinsic parameters and camera calibration factors and obtain rectification mapping data. The mapping data includes coordinate information that moves pixels on the original image to the rectified image. This procedure processes in software environment. And the rectification procedure compensates input images using mapping data from the LUT memory. Since complex computation is mostly calculated in the calibration procedure, the rectification procedure could be designed compact hardware architecture and be suitable for real-time processing. However, there are four different mapping data set which are X and Y coordinate information from left and right images. And it affects high memory consumption. Therefore, each mapping data set ought to be compressed. Compressed LUT methods are simply added encoding and decoding parts before and after LUT memory, respectively. And complexity increase depends on which compression method is utilized. Compressed LUT methods classify loss and lossless compression. Figure 2 shows overall flow of rectification using LUT

A. *Loss compression*

The loss compressed LUT method usually applies down-sampling to reduce a size of LUT in the encoding process and interpolation to fill void pixels in the decoding process as in [9], [10]. Given that interpolation change calculated values based on relationship with adjacent values, a rectified image is distorted. Although rectified image using a loss compressed LUT shows reasonable PSNR over 30 dB, it could occur critical errors in the disparity estimation process. To avoid potential errors, the lossless compression is more suitable.

B. *Lossless compression*

The lossless compressed LUT method utilizes lossless compression technique such as Huffman, differential, run-length and etc. Among them, a differential encoding method is used with high compression ratio and compact hardware architecture as in [11]. It shows good trade-off between complexity and compression ratio. However, since it limits differential magnitude of sequential pixel values on 3 to minimize memory consumption, an error is occurred on the current coordinate if magnitude of differential value is more than 4. Moreover, when one error is occurred, it is propagated on the current line by accumulation of erroneous difference. Therefore, the previous differential encoding method operates properly only with low warping movement.

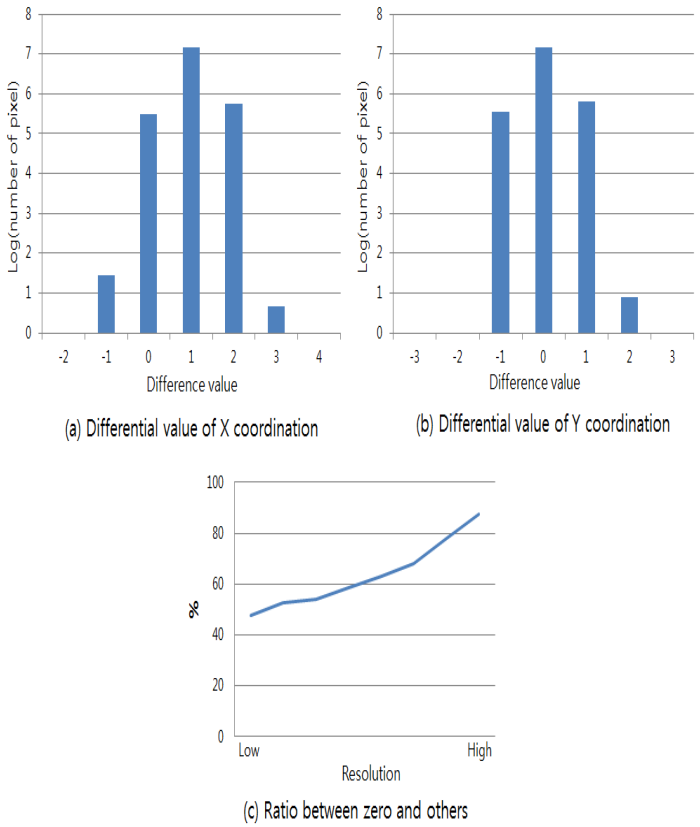

Fig. 3. Distribution of difference values (a) differential values of X coordinate (b) differential values of Y coordinate (c) ratio between the highest probability case and others.

III. Proposed Algorithm

Adaptive compression method basically uses characteristic of input. Reference [18] adjusted sampling frequency depend on frequency of ECG (electrocardiogram) signal. Especially, ECG signal with low frequency sampled with low sampling frequency, which decrease amount of data. In the same manner, our proposed method adjusted size of memory bits to store coordinate data depend on magnitude of differential values. Size of memory bits is minimized to decrease compression ratio for the highest probability case and also maximized to have enough bit size to store maximum magnitude for the opposite case. Therefore, compression ratio is decreased with increasing the highest probability case.

As shown in figure 3(a) and 3(b), variance of differential coordinate values from 50 stereo image sets is distributed around 1, 0 for X and Y coordinate, respectively. Moreover, as shown in figure 3(c), since the ratio between the highest probability case and others increases with higher resolution, our proposed method is more suitable for higher resolution. To satisfy above-mentioned conditions, we composed two codebooks as shown in table 1.

TABLE I
Two Codebooks for Adaptive Binary Encoding

Codebook I		
Range of magnitude	1 for x axis 0 for y axis	-1, 0 ,2, 3 for x axis -2, -1, 1, 2 for y axis
Mode bit	0	1
Sign bit	-	1 bit
Magnitude bit	-	1 bit
Total bit	1 bit	3 bits

Codebook II				
Range of magnitude	0	±1~ ±2	±3~ ±6	±7~
Mode bit	00	01	10	11
Sign bit	-	1 bit	1 bit	1 bit
Magnitude bit	-	1bit	2 bits	3 bits~
Total bit	2 bits	4bits	5 bits	6 bits~

The codebook I is used for small magnitude, which consists of two modes. The first mode is for the highest probability case; 1 for x axis, 0 for y axis. And the second mode encodes rest of cases. The codebook II is used for large magnitude, which consists of four modes. The difference value that has the highest probability case sets as mode ‘00’ to decrease compression ratio. And to cover larger range of magnitude, the codebook could rearrange by expansion of magnitude bit in mode ‘11’.

Let’s assume that we have differential value 0 and -5 in y axis. First, 0 is able to encode with two codebooks. In the codebook I, 0 in the y axis is in the mode ‘0’. And mode ‘0’ has no sign bit and magnitude bit. Therefore, 0 is encoded as ‘0’. On the other hands, in the codebook II, 0 is included in mode ‘00’. And mode ‘00’ is the same as mode ‘0’ in the codebook I. Therefore, 0 is encoded as ‘00’. Second, -5 cannot be encoded using the codebook I due to large magnitude. However, the codebook II can encode -5 that is included in mode ‘10’. Sign is minus and magnitude is 5. We can assign mode bit as ‘10’, sign bit as ‘1’, magnitude bit as ‘10’. Therefore, -5 is encoded as ‘10110’. Our proposed method chooses a proper codebook based on magnitude. Selected codebook is stored to the codebook table register in the decoder. The encoding flow is shown in figure 4.

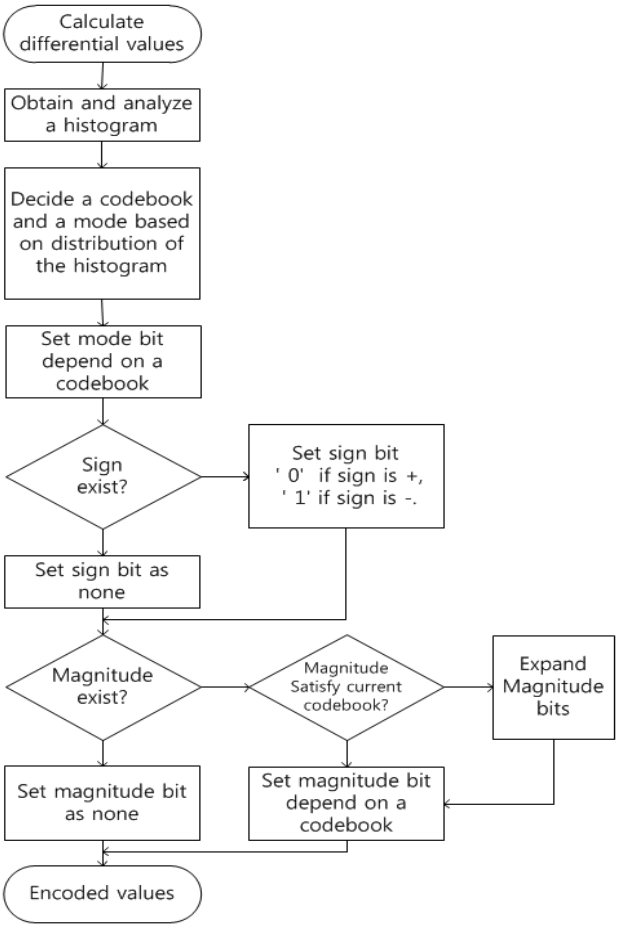

Fig. 4. Encoding flow

IV. Proposed Hardware Architecture

Our proposed hardware architecture consists of LUT memory, a decoder and a pixel address generator. First, the decoder reads differentially encoded data from LUT memory and decode into X and Y coordinate values. Then the pixel address generator reconstruct X and Y coordinate values into pixel address on the original image. The decoder consists of data controller and codebook table registers and the pixel address generator consists of one accumulator for X coordinate, one accumulators and one multiplier for Y coordinate and one adder to combine X and Y coordinate values. Overall hardware architecture is compact with low latency and simple computation, which is suitable for real-time processing.

Decoding flow is processed as followings. First, each data controller obtains the information about which codebook is used and reads encoded data from LUT memory. Second, data is decoded from the binary codes to the differential values using the stored codebook. Lastly, we accumulate differential values to decode into coordinate values, and generate pixel addresses. The proposed hardware architect is shown in fig. 5.

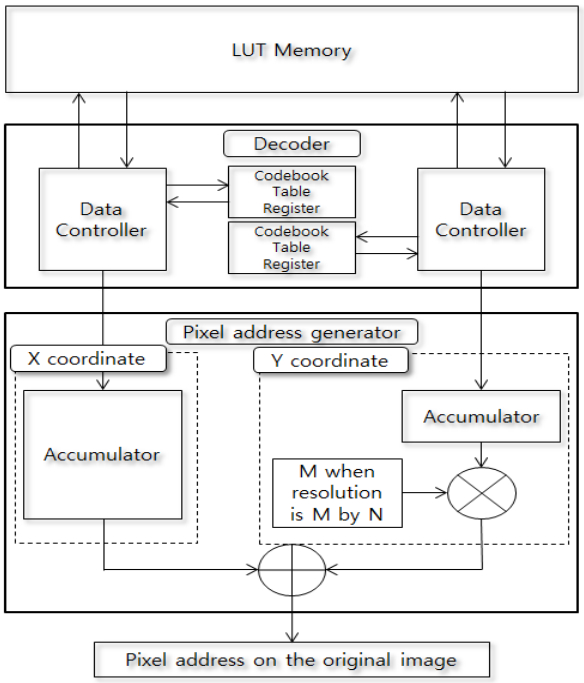

Fig. 5. Proposed hardware architecture

V. Experimental Result

Our proposed method is designed using OpenCV for the encoding process and Verilog for the decoding process. For the evaluation, we applied two methods. The first one is a binary image of difference to show distortion. The equation for binarization is as:

$$B(x,y) = \begin{cases} 0, & Rect_{img}(x,y) = Ori_{img}(x,y), \\ 1, & Rect_{img}(x,y) = Ori_{img}(x,y). \end{cases} \quad (1)$$

Since distortion is the same as difference, distortion regions represent with white pixels in the result images. As shown in figure 6, the result images of the loss compression method have white regions, whereas our proposed method does not.

(a) Rectified results

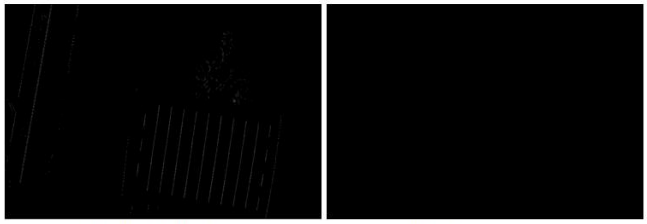

(b) Differential binary image using abstract encoding[9]

(c) Differential binary image using proposed encoding

Fig. 6. Differential binary image

The second method is compression ratio. Compression ratio (CR) is defined as:

$$CR = \frac{Compressed\ data}{Uncompressed\ data} \quad (2)$$

We compared to previous differential encoding method as in [11] and two codebooks with various resolution conditions and 50 stereo image sets. As shown in figure 7, compression ratio of our proposed method has minimum 18.9% and maximum 26.1% lower than the previous one. And difference of compression ratio in the same resolution becomes larger with higher resolution.

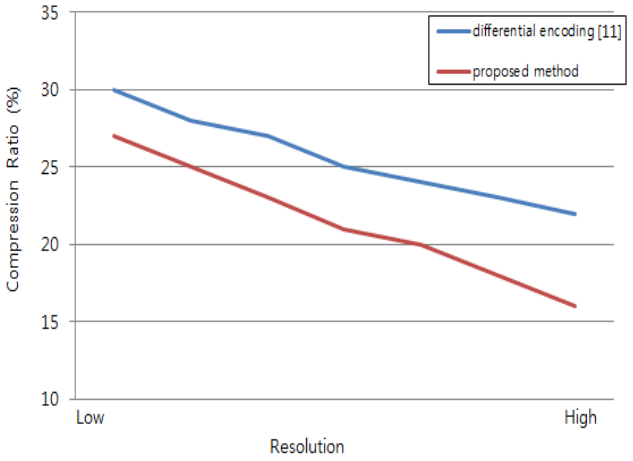

Fig. 7. Compression ratio results with various resolutions

As shown in figure 8, differential encoding shows only 31.69% compression ratio regardless of stereo environment due to fixed encoding bits. On the other hands, our proposed methods show different results as per stereo environment, since it has different encoding bits depend on modes. And for performance, our proposed methods have approximately two-third and one-third lower compression ratio with the codebook II and the codebook I, respectively.

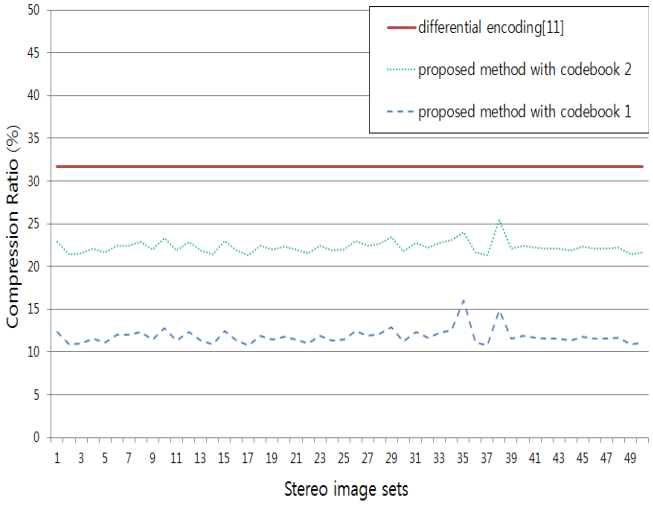

Fig. 8. Compression ratio results with 50 stereo image sets

VI. Conclusion

In this paper, we proposed an adaptive differential encoding method for high-resolution video. Our proposed method effectively encodes satisfying two conditions such as minimization to decrease compression ratio and maximization to tolerate large magnitude values. And decoding process also achieves compact hardware architecture with processing in real-time. Compression ratio is approximately from 10.8% to 26.1% depending on resolution with no distortion. And the higher resolution shows the lower compression ratio which is suitable for image processing with high-resolution.

REFERENCES

[1] Yunseok Lee, Kar-Ann Toh and Sangyoun Lee, "Stereo image rectification based on polar transformation," *Optical Engineering*, 47(8), 087205, 2008.

[2] Nicholas Ayache and Charles Hansen, "Rectification of Images for Binocular and Trinocular Stereovision," *in Proc. Pattern Recognition*, vol. 1, pp. 11-16, Nov, 1988.

[3] Marc Pollefeys, Reinhard Koch and Luc Van Gool, "A Simple and Efficient Rectification method for General Motion," *in Proc. Computer vision*, vol. 1, pp 496-501, Sep, 1999.

[4] Andrea Fusiello, Emanuele Trucco and Alessandro Verri, "A Compact Algorithm for Rectification of Stereo pairs," *Machine Vision and Applications*, Vol. 12, pp. 16-22, 2000.

[5] S. Jin, J. Cho, X. D. Pham, K. M. Lee, S. K. Park, M. Kim and J. W. Jeon, "FPGA Design and Implementation of a Real-time Stereo Vision System," *IEEE Trans. Circuits and Systems for Video technology*, Vol. 20, No. 1, pp. 15-26, Jan, 2010.

[6] Minsu Choi, Jinsang Kim, Won-Kyung Cho and Yunmo Chung, "Low Complexity Image Rectification for Multi-view Video Coding," *in Proc. ISCAS 2012*, pp. 381-384, May, 2012.

[7] Heiko Hubert, Benno Stabernack and Frederik Zilly, "Architecture of a Low Latency Image Rectification Engine for Stereoscopic 3-D HDTV Processing," *IEEE Trans. Circuits and Systems for Video technology*, Vol. 23, No. 5, pp. 813-822, May, 2013.

[8] Cristian Vancea and Sergiu Nedevschi, "LUT-based Image Rectification Module Implemented in FPGA," *in Proc. Intelligent Computer Communication and Processing*, pp. 147-154, Sep, 2007.

[9] Anders Kjaer-Nielsen, Lars Baunegaard With Jensen, Anders Stengaard Sorensen and Norbert Kruger, "A Real-time Embedded System for Stereo Vision Preprocessing using an.FPGA," *in Proc. Reconfigurable Computing and FPGAs*, pp. 37-42, Dec, 2008.

[10] Khurram Jawed, John Morris, Tariq Khan and Georgy Gimel'farb, "Real time Rectification for Stereo Correspondence," *in Proc. Computational Science and Engineering*, pp. 277-284, Aug, 2009.

[11] Deuk Hyun Park, Hyoung Seok Ko, Jae Gon Kim and Jun Dong Cho, "Real Time Rectification using Differentially Encoded Lookup Table," *in Proc. ICUIMC 2011*, No. 47, Feb, 2011.

[12] Abdulkadir Akin, Ipek Baz, Luis Manuel Gaemperle, Alexandre Schmid and Yusuf Leblebici, "Compressed Look-Up-Table based Real-Time Rectification Hardware," *in Proc. VLSI-SoC 2013*, pp. 272-277, Oct, 2013.

[13] Ayman F. Habib, Eui-Myoung Kim and Chang-Jae Kim, "New Methodologies for True Orthophoto Generation," *Photogrammetric Engineering & Remote Sensing*, Vol. 73, No. 1, pp. 25-36, Jan, 2007.

[14] W. Karel, M. Doneus, G. Verhoeven, C. Briese, C. Ressl, N. Pfeifer, "Oriental – Automatic Geo-referencing and Ortho-rectification of Archaeological Aerial Photographs," *ISPRS Annals of the Photogrammetry, Remote Sensing and Spatial Information Science*, Vol II-5/W1, 2013, XXIV International CIPA Symposium, Sep, 2013.

[15] Yun-Suk Kang, Cheon Lee and Yo-Sung Ho, "An Efficient Rectification Algorithm for Multi-view Images in Parallel Camera Array," *in Proc. 3DTV conference: The True Vision- Capture, Transmission and Display of 3D Video*, pp. 61-64, May, 2008.

[16] Wannes van der Mark and Dariu M. Gavrila, "Real-time Dense Stereo for Intelligent Vehicles," *IEEE Trans. Intelligent transportation systems*, Vol. 7, No. 1, March, 2006.

[17] Anwar Hasni Abu Hasan, Rostam Affendi Hamzah and Mohd Haffiz Johar, "Range Estimation in Disparity Mapping for Navigation of Stereo Vision Autonomous Vehicle using Curve Fitting Tool," *IJVIPNS*, Vol. 9, No. 9, pp. 5~9, Oct, 2009.

[18] Zhongyun Yuan, Jong-hak Kim and Jun-dong Cho, "Adaptive Sampling for ECG Detection based on Compression Dictionary," *JSTS*, Vol. 13, No. 6, DEC, 2013.

Jong-hak Kim received the B.S. degree in radio communication engineering from the Kyunghee University, Suwon, Korea, in 2009, the M.S. degree from the Department of Electrical and Computer Engineering, Sungkyunkwan University, in 2012, and he is studying for a Ph. D degree at Sungkyunkwan University.

He is interested in the efficient low power hardware implementation for a real-time image processing system in mobile equipment. He currently studies a visual fatigue reduction scheme for a stereo vision system.

Jung-kyun Oh received the B.S degree in Information Communication Engineering from Myongji University, Yongin, Korea, in 2009. He is a M.S candidate in the Human ICT Convergence Department at Sungkyunkwan University, Suwon, Korea.

His research interests include SoC for 3D Image Processing Applications and 3D visual fatigue reduction.

Seong-muk Kang received the B.S degree from the Department information communication from Baekseok University, Korea, in 2013. And he is studying for a master's degree in Electrical Engineering at Sungkyunkwan University, Suwon, Korea.

His current research interests include image stabilization and stereo vision.

Jun-Dong Cho received the B.S. degree from the Department of Electronic Engineering, Sungkyunkwan University, Suwon, Korea, in 1980, the M.S. degree from the Department of Computer Science, Polytechnic University Brooklyn, New York, in 1989, and the Ph.D. degree from the Department of Computer Science, Northwestern University, Evanston, in 1993.

He was working for Samsung Electronics Company for 6 years. He joined the Department of Electrical and Computer Engineering, Sungkyunkwan University (SKKU), Suwon, Korea, since 1995, where he is currently chair of graduate school of Human ICT Convergence.

His research interests include Low Power Design, 3-D Image Processor, Embedded Multimedia, and Human ICT Application.

Prof. Cho is an IEEE Senior Member.

Volume 3 Issue 6, Nov. 2014, ISSN: 2288-0003

ICACT-TACT JOURNAL

Global IT Research Institute

1713 Obelisk, 216 Seohyunno, Bundang-gu, Sungnam Kyunggi-do, Republic of Korea 463-824

Business Licence Number : 220-82-07506, Contact: secretariat@icact.org Tel: +82-70-4146-4991